

# Resolving sea ice dynamics in the north-western Ross Sea during the last 2.6 ka: From seasonal to millennial timescales

T. Tesi <sup>a,\*</sup>, S.T. Belt <sup>b</sup>, K. Gariboldi <sup>c</sup>, F. Muschitiello <sup>d</sup>, L. Smik <sup>b</sup>, F. Finocchiaro <sup>e</sup>, F. Giglio <sup>a</sup>, E. Colizza <sup>e</sup>, G. Gazzurra <sup>c</sup>, P. Giordano <sup>a</sup>, C. Morigi <sup>c,f</sup>, L. Capotondi <sup>g</sup>, A. Nogarotto <sup>h</sup>, D. Köseoğlu <sup>b</sup>, A. Di Roberto <sup>i</sup>, A. Gallerani <sup>g</sup>, L. Langone <sup>a</sup>

<sup>a</sup> Istituto di Scienze Polari - Consiglio Nazionale delle Ricerche ISP-CNR, Via P. Gobetti 101, 40129, Bologna, Italy

<sup>b</sup> Biogeochemistry Research Centre, School of Geography, Earth and Environmental Sciences, University of Plymouth, Drake Circus, Plymouth, Devon, PL4 8AA, UK

<sup>c</sup> Dipartimento di Scienze della Terra, Università di Pisa, Via Santa Maria, 53, 56126, Pisa, Italy

<sup>d</sup> Department of Geography, University of Cambridge, Cambridge, CB2 3EN, UK

<sup>e</sup> Dipartimento di Matematica e Geoscienze, Università di Trieste, Via E. Weiss 2, 34127, Trieste, Italy

<sup>f</sup> Geological Survey of Denmark and Greenland (GEUS), Øster Voldgade 10, 1350, København, Denmark

<sup>g</sup> Istituto di Scienze Marine - Consiglio Nazionale delle Ricerche ISMAR-CNR, Via P. Gobetti 101, 40129, Bologna, Italy

<sup>h</sup> Campus Scientifico, Università Ca' Foscari Venezia, Via Torino 155, 30172, Venezia, Mestre, Italy

<sup>i</sup> Istituto Nazionale di Geofisica e Vulcanologia (INGV), Sezione di Pisa, Via della Faggiola 32, 56126, Pisa, Italy

## ARTICLE INFO

### Keywords:

Ross sea

Fast ice

Laminated sediments

IPSO<sub>25</sub>

Sea ice

## ABSTRACT

Time-series analyses of satellite images reveal that sea ice extent in the Ross Sea has experienced significant changes over the last 40 years, likely triggered by large-scale atmospheric anomalies. However, resolving how sea ice in the Ross Sea has changed over longer timeframes has until now remained more elusive. Here we used a laminated sediment piston core (14.6 m) collected from the Edisto inlet (Western Ross Sea) to reconstruct fast ice dynamics over the last 2.6 ka. Our goal was to first understand the climate expression of selected well-defined sediment laminae and then use these characteristics for reconstructing past sea ice behaviour across the whole sedimentary sequence. We used the recently established sea ice diatom biomarker proxy IPSO<sub>25</sub> in combination with diatom census counts and bulk analyses. Analyses performed on a suite of discrete laminae revealed statistically significant differences between dark and light laminae reflecting different depositional conditions. Based on their respective biogeochemical fingerprints, we infer that dark laminae accumulated during sea ice thaws in early summer. Under these conditions, laminae contain relatively high concentrations of IPSO<sub>25</sub> and display an enriched  $\delta^{13}\text{C}$  composition for the bulk organic matter (OM). While diatom assemblages in dark laminae are relatively homogenous, as the thaw continues later in the summer, *Corethron pennatum* becomes the dominant diatom species, resulting in the formation of light laminae characterized by low IPSO<sub>25</sub> concentrations. Since *C. pennatum* can migrate vertically through the water column to uptake nutrients and avoid competition in oligotrophic waters, its high concentration likely reflects stratified and ice-free surface waters typical of late summer.

Down-core trends show that the correlation between sediment brightness and geochemical fingerprint (i.e., IPSO<sub>25</sub> and  $\delta^{13}\text{C}$ ) holds throughout the record. Based on the knowledge gained at lamina level, our down-core high-resolution reconstruction shows that the summer fast ice coverage changed dramatically during the late Holocene. Specifically, we conclude that the Edisto inlet experienced regular early summer opening between 2.6 ka, and ca. 0.7 ka, after which, coastal fast ice persisted during summer months and ice-free conditions became less frequent. Comparison with previous regional ice core data suggests that the sudden cooling recorded over the Victoria Land Coast region since 0.7 ka might potentially explain our observation of persistent summer fast ice in the Western Ross Sea. Our study has shown that multi-proxy data derived from laminated sediments can provide hitherto unknown detail regarding past summer sea ice dynamics in coastal Antarctic regions.

\* Corresponding author.

E-mail address: [tommase.tesi@cnr.it](mailto:tommase.tesi@cnr.it) (T. Tesi).

## 1. Introduction

Since multichannel passive-microwave satellite records began in the late 1970's, it has become evident that Antarctic sea ice extent has exhibited sub-regional patterns. Various mechanisms have been proposed to explain such spatial variability, including the El Niño–Southern Oscillation (Stammerjohn et al., 2008), the Interdecadal Pacific Oscillation (Meehl et al., 2016), the Amundsen Sea Low (Turner et al., 2009), as well as basal melting of Antarctic ice shelves (Bintanja et al., 2013). Despite these diverse explanations, the collective picture indicates that Antarctic sea ice distribution is expressed by large-scale climate dynamics; in turn, sea ice regulates fundamental aspects of global climate (e.g. thermohaline circulation, ocean-atmosphere heat/gas exchange and radiative properties). However, a survey of the current literature clearly reveals that our knowledge of sea ice-climate interactions in the Southern Ocean essentially relies on the last 40 years of satellite imagery, with longer-term records far more elusive because of the paucity of sea ice archives.

In this study, we demonstrate the suitability of laminated sedimentary units for the reconstruction of past sea ice dynamics in Antarctica. Laminated diatom ooze deposits have been documented in different regions of the Antarctic margin, including the Antarctic Peninsula (Bahk et al., 2003; Hjort et al., 1997; Leventer et al., 2002; Maddison et al., 2005), the East Antarctic Margin (Alley et al., 2018; Denis et al., 2006; Maddison et al., 2006, 2012), and the Ross Sea (Finocchiaro et al., 2005; McKay et al., 2016). Such laminated records often reflect weak post-depositional reworking, which makes them suitable archives for resolving seasonal and sub-seasonal processes driven by short-lived climate variability. Although the formation of laminated units is dependent on local and regional conditions, collectively, their deposition is generally attributed to spring and summer algal bloom events associated with seasonal sea ice retreat (Abram et al., 2014; Finocchiaro et al., 2005; Leventer et al., 2002; Maddison et al., 2012). As such, analysis of such laminated sediments using appropriate proxy signatures of the respective bloom events has the potential to provide insights into local sea ice dynamics (at least) and any changes to these over time.

In this study, we analysed laminated sediments from a piston core collected from the Edisto inlet (Western Ross Sea) (HLF17-1, Fig. 1; Fig. 2) to reconstruct past sea ice variability during the late Holocene (last ca. 2.6 ka) via an expanded record characterized by continuous diatom-rich laminations. Since the 1970s, sea ice has increased over the Ross Sea, followed by rapid negative anomalies in recent years (e.g. 2016) (Parkinson, 2019; Turner et al., 2017). The reasons behind the strong variability of sea ice in the Southern Ocean is a matter of on-going discussion, although compiled evidence suggests that there are likely multiple factors that collectively involve anomalies in the atmospheric and, consequently, oceanic circulation (Meehl et al., 2019). Our study focuses on land-fast ice dynamics, which is a major sea ice type common to Antarctic coastal regions. Sea ice reconstructions have traditionally been based on ecological proxies such as diatom assemblages, whose relative abundance in Antarctic sediments reflects changes in sea surface conditions (Armand et al., 2005; Gersonde and Zielinski, 2000; Leventer, 1998). Over the last decade, sea ice diatom-produced Highly Branched Isoprenoid (HBI) lipids have emerged as novel biomarker proxies for Arctic and Antarctic sea ice (Belt, 2018, 2019; Belt and Müller, 2013; Collins et al., 2013; Massé et al., 2011; Vorrath et al., 2019). For the Southern Ocean, the diunsaturated HBI termed IPSO<sub>25</sub> (“Ice Proxy for the Southern Ocean with 25 carbon atoms”) has been suggested as a biomarker of land-fast ice. In a preliminary study (Belt et al., 2016), it was suggested that this source-specific HBI might trace the occurrence of the sympagic (*i.e.* living within sea ice) diatom *Berkeleya adeliensis*,

which flourishes predominantly in the bottom sections of fast ice and within the underlying platelet ice (Riaux-Gobin et al., 2013). Otherwise, unlike its close structural counterpart IP<sub>25</sub> in the Arctic (see Belt, 2018 for a recent review), there have been no in-depth investigations into the relationship between IPSO<sub>25</sub> distributions and Antarctic sea ice characteristics (e.g. sea ice concentration, ice type, presence of polynyas, etc.). A relatively small number of Holocene sea ice reconstructions based on IPSO<sub>25</sub> have assumed a positive relationship between sedimentary IPSO<sub>25</sub> concentration and sea ice extent in a general sense, an interpretation supported in some cases by diatom assemblage data (Denis et al., 2010; Etourneau et al., 2013; Lamping et al., 2020; Massé et al., 2011). Finally, in a recent pilot study of surface sediments from the West Antarctic Peninsula, Vorrath et al. (2019) concluded that a number of different factors likely need to be considered when using IPSO<sub>25</sub> (and combined biomarker indices based on IPSO<sub>25</sub>) for paleo sea ice reconstruction, especially given the complex nature of Antarctic sea ice dynamics. As such, it seems likely that the use of IPSO<sub>25</sub> as a sea ice proxy needs to be carried out on a context-specific, rather than a generic, basis.

This study presents the first high-resolution reconstruction of late-Holocene sea ice dynamics in the Western Ross Sea inferred from IPSO<sub>25</sub>. Among its various attributes, the comparatively time-efficient analysis of IPSO<sub>25</sub> makes it an ideal tool to be used in high-resolution studies dealing with laminated sequences. However, since IPSO<sub>25</sub> is still a relatively new proxy (see Belt, 2018 for a review) and the likely need to use it according to the specific sea ice setting (see above), our study also involves the analysis of some diatom assemblages and other complementary biogeochemical and lithological parameters, which include the stable isotopic composition of bulk organic carbon, inorganic elemental composition, and grain size measurements.

The overarching objectives of this study were threefold: (i) to investigate the extent to which proxy data obtained from dark and light laminae found in HLF17-1 reflected annual, seasonal or sub-seasonal fast ice dynamics; (ii) to use this information to infer the millennial-scale variability of sea ice in the inner-shelf of the Ross Sea over the last 2.6 ka BP; (iii) to rationalise findings through consideration of other climatic parameters pertinent to the late Holocene.

## 2. Regional setting

Edisto Inlet is a small ice-filled elongated NNE-SSW fjord situated behind Cape Hallett, along the Victoria Land Coast in the north-western Ross Sea. The fjord is approximately 15 km long and 4 km wide, with a maximum water depth of approximately 500 m and a sill 400 m deep, which divides the fjord from Moubay Bay to the north. Geophysical data (3.5 kHz sub-bottom profiler) acquired during the 2005 PNRA (National Antarctic Research Program) Italian expedition highlighted that the studied core was collected in a very expanded Holocene sequence characterized by soft biogenic laminated sediments (Fig. 1c).

## 3. Materials and methods

### 3.1. Sampling and subsampling

Piston core HLF17-1 (72° 18.4842' S - 170° 03.2592' E; 465 m water depth) was collected in February 2017 in the Edisto inlet on board of the *R/V Italica* (Fig. 1). The core, 14.65 m long, was split into 1-m long sections and stored at 4 °C on the vessel. At the same site, a box core (HLF17-2BC, 56 cm) was retrieved and kept refrigerated under the same conditions as the piston core. In the laboratory, open core sections were analysed using an AVAATECH core scanner

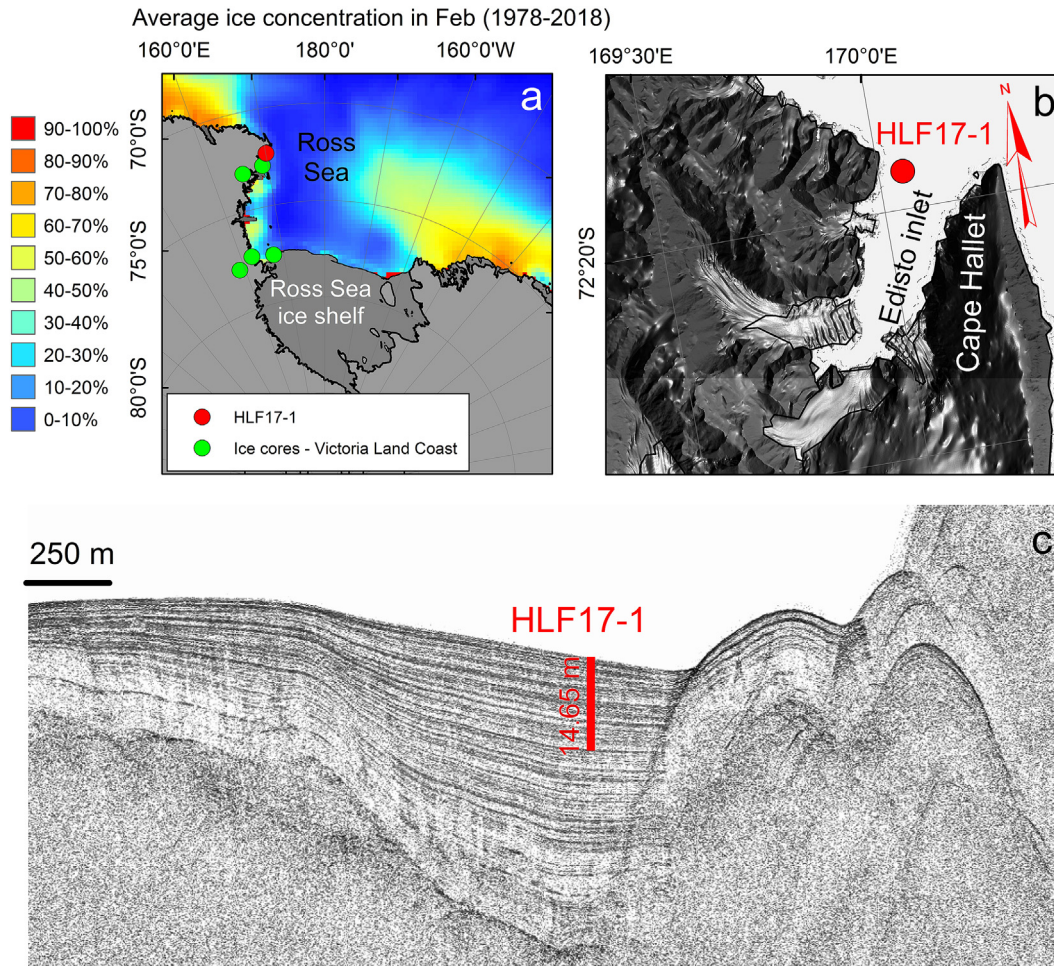


**Fig. 1.** Study area in the Ross Sea. (a) Map showing the 40-y average of sea ice concentration (%) in February based on satellite images. The locations of HLF17-1 core and ice cores of the Victoria Land Coast are shown with filled red and green circles, respectively; (b) Red filled circle shows the location of HLF17-1 in the Edisto inlet; (c) Chirp profile showing the sediment strata geometry. Parallel reflectors show continuous sedimentation throughout the Holocene. (For interpretation of the references to colour in this figure legend, the reader is referred to the Web version of this article.)

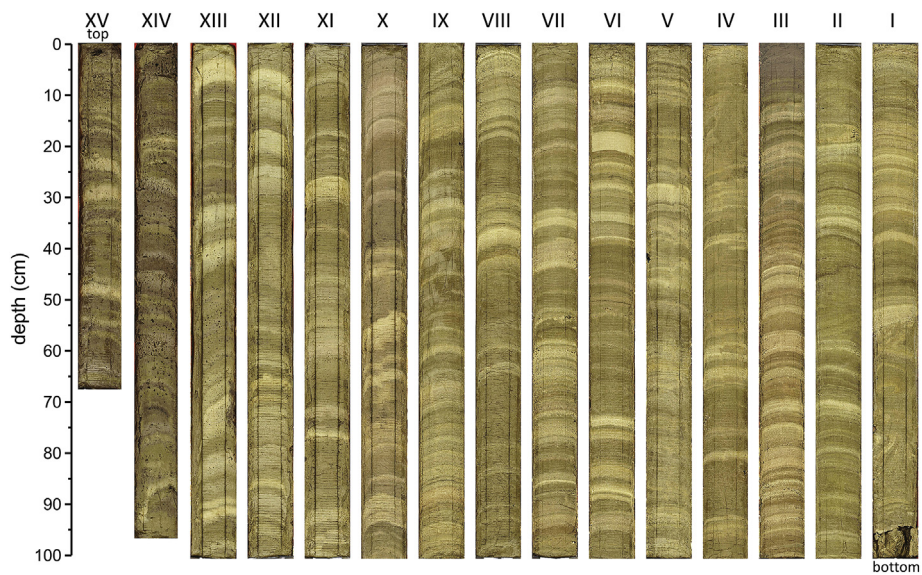


**Fig. 2.** HLF17-1 piston core (14.65 m) from top (section XV) to bottom (section I)

for high-resolution image acquisition and XRF analyses (0.5-cm sampling interval). Sediments were sub-sampled throughout every 5 cm at 1–2 cm thick intervals ( $n = 295$ ), while distinct laminae ( $n = 34$ ) were subsampled from [section III](#). All subsamples were frozen and freeze-dried prior to analysis.

The HLF17-1 core site was visited previously in 2016 on board the *R/V Italica*, during which time a 11.43 m long core (HLF16-1) was retrieved and split into sections as described above. Unfortunately, freezing of the core due to failure of the cooling system resulted in the expansion and loss of sediments from the liner ends. Despite this handling issue, the stratigraphy of remaining sediments was well preserved. HLF17-1 and HLF16-1 were correlated with each other using distinctive lamination patterns (Supplementary Material, [Fig. S1](#)). HLF16-1 was then sub-sampled (10-cm thick intervals) and wet-sieved to isolate carbonate microfossils for the age-depth model of HLF17-1.

### 3.2. Bulk analyses

Freeze-dried samples were powdered and homogenized in an agate mortar. Acidified sediments (1.5 M HCl) were analysed using a Thermo Fisher Elemental Analyser (FLASH, 2000 CHNS/O) coupled with a Thermo Finnigan Delta plus isotope ratio mass spectrometer (IRMS) for organic carbon (OC, wt.%), total nitrogen (TN, wt.%) and stable carbon isotopes ( $\delta^{13}\text{C}$ , ‰) ([D'Angelo et al., 2018](#); [Tesi et al., 2012](#)). Opal content (wt.%) was measured according to the leaching method developed by [Mortlock and Froelich \(1989\)](#). Sediments were placed in Teflon tubes and alkaline dissolution was performed with 0.5 M  $\text{Na}_2\text{CO}_3$  solution at 80 °C for 5 h. Dissolved silica was measured according to the molybdate-blue spectrophotometric method ( $\lambda = 812$  nm). Data are reported as weight percentage (wt.%) of  $\text{SiO}_2 \times (0.4\text{H}_2\text{O})$ .

Major (%) and minor (ppm) elements were quantified using a wavelength dispersive Philips PW 1480 sequential X-ray fluorescence spectrometer (XRF). Analyses were carried out on pressed powder pellets applying the matrix correction as presented in [Dinelli et al. \(2001\)](#). Aliquots designated for XRF were used to make loss-on-ignition (LOI, 950 °C) measurements. The reproducibility for major and minor elements was ca. 7% and 5%, respectively, and shifted to ca. 15% for minor elements <10 ppm ([Dinelli et al., 2001](#)). In this study, only the major lithogenic elements are presented ( $\text{SiO}_2$ ,  $\text{Al}_2\text{O}_3$ ,  $\text{TiO}_2$ ,  $\text{Fe}_2\text{O}_3$  and  $\text{K}_2\text{O}$ ; the remaining XRF data can be found in the Supplementary Material). XRF analyses were performed exclusively on light and dark laminae sub-sampled from [section III](#).

The grain-size of each bulk sediment sample was determined using a Malvern Mastersizer Hydro 2000S Diffraction Laser unit for the <2 mm size fraction. Sand, silt and clay fractions were determined using the grain-size classification proposed by [Wentworth and Chester \(1922\)](#).

All bulk data not discussed in detail in the main text are presented in the Supplementary Material.

### 3.3. HBIs

Sediments were extracted, purified and analysed using the analytical method described previously ([Belt et al., 2019](#)). Briefly, prior to extraction, 9-octylheptadec-8-ene (9-OHD; ca. 0.1  $\mu\text{g}$ ) was added to sediments as an internal standard to enable quantification of IPSO<sub>25</sub> by gas chromatography–mass spectrometry (GC–MS). Sediments were subsequently saponified in methanolic KOH ( $\text{H}_2\text{O}/\text{MeOH}$ , 1:9; 5% *m/v* KOH) for 60 min at 70 °C. After extraction with hexane (3 × 3 ml), the centrifuged supernatant containing HBIs was dried under a  $\text{N}_2$  stream. The dry extract was re-dissolved in hexane (500  $\mu\text{l}$ ) and purified using open column chromatography ( $\text{SiO}_2$ ,

38–63  $\mu\text{m}$ ). The eluted hexane fraction (3 × 2 ml) was dried under a  $\text{N}_2$  stream and re-dissolved in 300  $\mu\text{l}$  of hexane prior to GC–MS analysis.

HBIs were quantified via GC–MS using an Agilent 7820a chromatograph fitted with a J&W DB5-MS column (30 m length, 0.25 mm i. d., 0.25  $\mu\text{m}$  film thickness) coupled to a 5977b Mass Selective Detector (MSD). The oven temperature ramp was programmed from 60 °C to 280 °C at 10 °C/min. During the ramp, the MSD operated in both Selective Ion Monitoring (SIM) and SCAN modes.

The sea ice algae-derived biomarker IPSO<sub>25</sub> (HBI diene II) and a tri-unsaturated HBI made by certain open water diatoms ([Belt et al., 2017](#)), referred to here as HBI III, were identified by comparison of their mass spectra with those published in previous studies ([Belt, 2018](#); [Belt et al., 2012](#)). The injection of  $\text{C}_8$ – $\text{C}_{40}$  alkanes (Sigma-Aldrich) was used to further check the retention indices of IPSO<sub>25</sub> and HBI III. Quantification of IPSO<sub>25</sub> and HBI III ([Fig. S2](#)) was achieved by integrating peaks of ions *m/z* 348.3 and 346.3, respectively, in SIM mode followed by normalizing to the corresponding peak area of the internal standard (9-OHD) and an instrumental response factor obtained by analysis of a purified standard. Data are presented as ng/g opal since both biomarkers are only produced by diatoms and to circumvent the effect from dilution with lithogenic particles and other sources of OC. For example, other algae common to Antarctica such as *Phaeocystis Antarctica* are within the non-silica (and non-HBI) producing *Prymnesiophyte* class, and may potentially contribute to the total OC ([Arrigo et al., 2000](#); [Arrigo and van Dijken, 2004](#)). Normalisation of IPSO<sub>25</sub> to the opal content thus eliminates such possible types of dilution effect. In any case, we also provide our HBI biomarker data in ng/g OC and ng/g dry sediment in the Supplementary Material ([Figs. S3 and S4](#)).

### 3.4. Diatom analyses

An aliquot of each dry sediment (ca. 0.2 g) was treated in a beaker containing a solution of distilled  $\text{H}_2\text{O}$  (40 ml for each sample),  $\text{H}_2\text{O}_2$  (60 ml for each sample; concentration 40%) to dissolve organic matter, and  $\text{Na}_4\text{P}_2\text{O}_7$  (100 mg) to disaggregate sediment particles. The suspensions were heated (70 °C; 45 min), followed by the addition of 10 ml of HCl (concentration 10%). Suspensions were then heated (70 °C; 15 min) and rinsed repeatedly with distilled water in order to reach a pH of ca. 5–6. Rinsing was performed every 8 h to allow diatoms to settle. The resulting suspensions were then reduced to a volume of 50 ml. A coverslip was placed inside a Petri dish and a known volume of suspended material (ca. 150–300  $\mu\text{l}$ ) was pipetted into it, together with distilled water in order to achieve a heterogeneous distribution of diatoms on the surface of the dish. After removing excess water, coverslips were glued to microscope slides using the Norland Optical Adhesive 61 (NOA61) and dried under UV light. At least 300 diatom frustules were counted for each slide following the method proposed by [Crosta and Koç \(2007\)](#), which revised [Schrader and Gersonde \(1978\)](#) and [Armand \(1997\)](#). *Corethron pennatum* was counted as one when more than half a valve was present. The relative abundance of each diatom species in a sample was calculated as the percentage of valves of a given species in relation to the total number of valves counted in each sample. In addition, relative biovolume contribution was calculated following the equation and individual biovolumes proposed for each species by [Alley et al. \(2018\)](#).

### 3.5. Chronology

A detailed description of HLF17-1 chronology is presented in [section 4.3](#). Here, we present the analytical methods used to

constrain the different dated horizons encompassed by the age-depth model (Table 1). The top of HLF17-1 core was dated using the short-lived radionuclide  $^{210}\text{Pb}$  (maximum penetration depth, Fig. S5).  $^{210}\text{Pb}$  activity was derived from its daughter nuclide  $^{210}\text{Po}$  via alpha spectrometry, following the procedure presented elsewhere (Frignani et al., 2005). XRF core scanning data (0.5 cm resolution) were used to identify possible cryptotephra layers within the core. A significant anomaly in some element ratios (i.e. Zr/Sr and Nb/Sr) was found at 136.5 cm corresponding to a peak in volcanic ash concentration (cryptotephra). The bulk layer was treated in  $\text{H}_2\text{O}_2$  (40% concentration) to dissolve organic matter and with HCl (10% concentration) to dissolve carbonate. Resulting sediment was impregnated in epoxy resin and the textures and composition of glass particles were studied at the *Istituto Nazionale di Geofisica e Vulcanologia, Sezione di Pisa* (INGV-Pisa) using a scanning electron microscope (SEM), Zeiss EVO MA coupled with Oxford-Aztec Energy EDS Analysis System. Standards of volcanic glass were analysed to test the accuracy of data during the SEM analyses (Fig. S6).

Radiocarbon dating of bulk OC ( $n = 5$ ) and carbonate samples ( $n = 6$ ) was performed via accelerated mass spectrometry (AMS) at The National Ocean Sciences Accelerator Mass Spectrometry (Woods Hole Oceanographic Institution, USA) and at the Poznan Radiocarbon Laboratory (Poland). The Bayesian age-depth model was constructed in R using the Bchron package (Haslett and Parnell, 2008).

### 3.6. Statistical analyses

T-tests were used to determine whether the populations of dark and light laminae were statistically different from each other at  $p < 0.01$  (Excel, Analysis ToolPak). When the variance was different among populations, we ran the test assuming unequal standard deviation. Complete linkage agglomerative hierarchical clustering (AHC) was carried out using IPSO<sub>25</sub>,  $\delta^{13}\text{C}$  (OM), and *C. pennatum* (% biovolume) as descriptive variables in order to determine their ability to separate light and dark laminae into distinct groups. Subsequently, the same explanatory variables were used to build a classification tree (CT) model via the Classification and Regression Trees (CART) algorithm of Breiman et al. (1984) to determine thresholds that best separated light and dark laminae. Primary and surrogate splits were considered, and the CT was pruned by maximizing classification accuracy after 10-fold cross-validation (Fig. S7).

## 4. Results and discussion

This section initially focuses on the origin of dark and light laminae, followed by the reconstruction of centennial-scale fast ice variability in the Edisto inlet throughout the late Holocene.

### 4.1. Dark and light laminae composition

Core HLF17-1 exhibited well-defined dark and light laminae on a mm-to cm-scale throughout the record. In order to understand the origin of laminations and their relationship with sea ice, we sub-sampled individual laminae from section III of core HLF17-1 ( $n = 34$ , Fig. 2) since these were sufficiently thick to be collected without cross-contamination from adjacent sections. Overall, *t*-test analyses of IPSO<sub>25</sub>, geochemical and taxonomic data revealed that dark and light laminae were statistically different from each other with, however, important differences depending on the parameter (Table 2).

For example, the mean IPSO<sub>25</sub> concentration was much higher in the dark laminae compared to the light laminae (Table 2;  $p < 0.01$ ) (Fig. 3b). We interpret this as an indication of the opening of the

inlet during the summer ice break-up following the spring sympagic bloom, resulting in relatively high IPSO<sub>25</sub> concentrations in the dark laminae. In contrast, we suggest that lighter sediments with low IPSO<sub>25</sub> reflect largely (later) ice-free conditions, with lower contributions from sympagic algae. Related inferences were made previously by Massé et al. (2011) following analysis of IPSO<sub>25</sub> in laminated near-surficial sediments from Adélie Land (East Antarctica). Thus, alternating IPSO<sub>25</sub> concentrations were identified in contrasting light/dark laminated sediment sections believed to represent varying seasonal input; however, the precise seasonal characteristics of the individual laminae were not confirmed as part of the study by Massé et al. (2011) and the relationship between IPSO<sub>25</sub> concentration and lamina colour/brightness was also not reported.

If our interpretations of variable IPSO<sub>25</sub> in laminated sections from core HLF17-1 are correct, the distribution of diatoms would be expected to follow the lamina colour in line with the IPSO<sub>25</sub> data. Instead, the *t*-test showed that, with the exception of *Fragilariopsis obliquocostata* ( $p < 0.01$ ), differences between dark and light laminae were not statistically significant for the species identified, and the differences observed for *F. obliquocostata* were, in any case, small (Table 2). This contrasts with a qualitative examination of the light laminae, which gave a visual impression of being dominated by *C. pennatum* mats when compared to the dark laminae. Similar observations were made by Alley et al. (2018) in laminated sediments collected in Iceberg Alley (East Antarctica). However, Alley et al. (2018) also noted that *C. pennatum* is a relatively large diatom, so its abundance, relative to the total number of organisms, can lead to underestimations with respect to biomass or biovolume.

Thus, once the relative concentrations of diatoms in core HLF17-1 were re-calculated on a biovolume basis (calculations based on Alley et al., 2018, Table 3), *C. pennatum* became the most abundant species in the light laminae (Fig. 3c; Table 3), supporting the visual qualitative examination, and low IPSO<sub>25</sub> concentrations, as predicted. In fact, since *C. pennatum* can adjust its buoyancy to uptake nutrients beneath the pycnocline, *C. pennatum*-rich sediments likely accumulate towards the end of the summer when surface waters are ice-free, well-stratified and nutrient depleted (Alley et al., 2018; Leventer et al., 2006; Salter et al., 2012), again, consistent with the low IPSO<sub>25</sub> values. In contrast, for dark laminae, where IPSO<sub>25</sub> is generally high, the deposition of phyto-detritus is likely associated with the progressive accumulation of sympagic diatoms, as fast ice retreats in early summer, in combination with the first algal blooms, as further evidenced by increases to well-known sea ice associated species such as *F. obliquocostata* and *F. curta* (Table 3).

Consistent with this interpretation, the average stable carbon isotopic composition ( $\delta^{13}\text{C}$ ) of the OM in the dark laminae was relatively enriched in  $^{13}\text{C}$  compared to the light laminae (Table 2;  $p < 0.01$ ) (Fig. 3d). Indeed, we propose that the isotopic fingerprint of laminae likely reflects the influence of variable sea ice cover on the overall photosynthetic fractionation of  $\text{CO}_2$ , especially since it is well-known that sea ice-derived OM is normally relatively enriched in  $^{13}\text{C}$  compared to OM produced in pelagic settings (Massé et al., 2011). Under normal  $\text{CO}_2$ -replete conditions, such as those associated with cold open waters, preferential uptake of  $^{12}\text{CO}_2$  during photosynthesis leads to isotopically light OM; however, within the confined environment of semi-enclosed sea ice,  $\text{CO}_2$  becomes a limiting substrate, with consequential reduction in isotopic fractionation and OM that becomes relatively enriched in  $^{13}\text{C}$  (Geilfus et al., 2014, 2015). This effect can be augmented by the formation of melt ponds and percolation of meltwater into the ice matrix during ice break-up, which can further decrease the dissolved  $\text{CO}_2$  concentration (Geilfus et al., 2015), while the uptake of “heavy” bicarbonate as an alternative carbon source further increases  $\delta^{13}\text{C}$

**Table 1**  
Dated horizons using AMS, <sup>210</sup>Pb and tephra layer.

core	horizon	depth (cm) <sup>a</sup>	depth range (cm)	type of sample	ID lab	dating method	age (y)	error (y)	modelled median age	minimum 95% CI	maximum 95% CI
HLF16-1	VII 0-10	402	±5	benthic forams <sup>b</sup>	Poz-110839	<sup>14</sup> C	2330 yBP	30	1083	927	1253.65
HLF16-1	VII 0-10	402	±5	ophiuroidae	Poz-110430	<sup>14</sup> C	2220 yBP	30			
HLF16-1	VII 0-10	402	±5	bulk OC	Poz-110836	<sup>14</sup> C	2890 yBP	30			
HLF16-1	IV 60-70	775	±5	benthic forams <sup>b</sup>	OS-147514	<sup>14</sup> C	2800 yBP	15	1589	1387.35	1778.65
HLF16-1	IV 60-70	775	±5	bulk OC	Poz-111163	<sup>14</sup> C	3210 yBP	35			
HLF16-1	I 70-80	1091	±5	benthic forams <sup>b</sup>	Poz-110838	<sup>14</sup> C	3200 yBP	30	2055.5	1853.45	2260
HLF16-1	I 75-75.5	1091.25	±0.25	ophiuroidae	Poz-110431	<sup>14</sup> C	3250 yBP	30			
HLF16-1	I 70-80	1091	±5	planktic forams	OS-147503	<sup>14</sup> C	3300 yBP	35			
HLF16-1	I 70-80	1091	±5	bulk OC	Poz-110837	<sup>14</sup> C	3875 yBP	30			
HLF17-2BC	0-1	0.5	±0.25	bulk OC	Poz-108920	<sup>14</sup> C	200 yBP	30			
HLF17-1	XV 8-10	9	±0.5	bulk OC <sup>b</sup>	OS-141035	<sup>14</sup> C	1940 yBP	15	58	5	134
HLF17-1	XV 18-20	19	±1	sediment <sup>b</sup>		<sup>210</sup> Pb	150 y before 2017	20	154	119	190
HLF17-1	XIV 72-73	136.5	±1	sediment <sup>b</sup>		tephra <sup>c</sup>	687	7	687	675	698
HLF17-1	I 90-91	1456	±0.5	bulk OC <sup>b</sup>	Poz-92969	<sup>14</sup> C	4220 yBP	50	2623.5	2353.8	2868.1

<sup>a</sup> Depth refers to HLF17-1.

<sup>b</sup> Used in the age depth model.

<sup>c</sup> Di Roberto et al. (2019).

(OM) values (Lehmann et al., 2004).

Previous studies have suggested that other factors can also regulate the  $\delta^{13}\text{C}$  of phytoplankton including nutrient availability, growth rate and morphology (i.e. volume/surface cell ratio) (Crosta et al., 2005; Popp et al., 1998, 1999). While we cannot comment on the quantitative importance of the first two aspects in the current context, we note that some previous in-situ and batch culture studies indicate that the fractionation of  $^{13}\text{C}$  during photosynthesis decreases with increasing volume/surface area ratio of the diatom cell (Crosta et al., 2005; Popp et al., 1998). However, in the current study, the most depleted  $\delta^{13}\text{C}$  values for OM were found in the light laminae dominated by *C. pennatum*, which is characterized by a high volume/surface area ratio. Together, these data support our hypothesis that the progressive increase in  $\text{CO}_2$  concentration in surface waters upon transitioning from ice-covered to ice-free conditions likely exerted first-order control on the  $\delta^{13}\text{C}$  signature of diatomaceous OM, with most depleted  $\delta^{13}\text{C}$  values aligned with light laminae associated with summer pelagic conditions. Conversely, dark laminae contain a higher contribution from  $^{13}\text{C}$ -enriched sympagic OM following ice break-up and higher IPSO<sub>25</sub>. Consistent with this, although we did not measure  $\delta^{13}\text{C}$  for IPSO<sub>25</sub> in the current study, this biomarker has been previously shown to be significantly  $^{13}\text{C}$ -enriched in both sea ice and sediments ( $\delta^{13}\text{C}$  = ca. -5 to -18‰; Belt et al., 2016, and references cited therein).

We note that the diatom *Berkeleya adeliensis* was not observed in any of the laminae analysed, despite the identification of IPSO<sub>25</sub> in all cases. This might be a result of the occurrence of production of IPSO<sub>25</sub> by other, as yet unidentified, sources; however, HBIs

(including IPSO<sub>25</sub>) are only produced by certain diatoms (see Belt, 2018 for a recent review) and none of the other species identified here (Table S1) are known to biosynthesise IPSO<sub>25</sub>. Alternatively, the absence of *B. adeliensis* in all laminae may simply reflect its poor preservation in the water column and in sediments (due to lightly silicified valves) following its release from fast ice, as reported previously (Riaux-Gobin et al., 2011; Tanimura et al., 1990). Indeed, Tanimura et al. (1990) showed that *B. adeliensis* can account for a large fraction of diatom assemblages in sea ice and melt ponds, yet is frequently absent in surface sediments due to dissolution. In addition, we note that some of the *C. pennatum* observed in the current study was present as fragmented frustules. On the other hand, IPSO<sub>25</sub> appears sufficiently stable in sediments to permit identification in sediments spanning the Quaternary, at least (Belt, 2018, 2019).

The distributions of lithogenic material are also consistent with the biogenic content and associated interpretations of dark and light laminae. Specifically, dark laminae, on average, showed higher concentrations of lithogenic elements, including  $\text{TiO}_2$ ,  $\text{Al}_2\text{O}_3$  and  $\text{Fe}_2\text{O}_3$ , and  $\text{K}_2\text{O}$ , compared to the light laminae (Table 2;  $p < 0.01$ ) (Fig. 3e). Following our interpretations based on IPSO<sub>25</sub> concentration, diatom assemblages and  $\delta^{13}\text{C}$  (OM), we suggest that the relatively higher lithogenic content in the dark laminae likely reflects the opening of the inlet, when fast ice thaws and releases mineral dust deposited on sea ice during the preceding months of the year (Atkins and Dunbar, 2009). In fact, according to Atkins and Dunbar (2009), the flux of dust that accumulates over the sea ice in McMurdo Sound (Ross Sea) decreases with increasing distance from the coast and accounts for a large fraction of the total

**Table 2**  
Composition of laminae from section III of HLF17-1. Data were grouped according to the lamina colour: light vs dark. Statistically significant differences between groups for each variable were assessed based on T-test ( $p < 0.01$ ).

laminae	depth cm	N <sub>tot</sub> %	OC %	$\delta^{13}\text{C}$ ‰	Opal %	porosity	IPSO <sub>25</sub> ng/g opal	sand %	silt %	clay %	Chaetoceros RS %	Corethron penmatum %	Fragilariopsis curta %	Fragilariopsis cylindrus %	Fragilariopsis obliquocostata %	Fragilariopsis separanda %	SiO <sub>2</sub> %	TiO <sub>2</sub> %	Al <sub>2</sub> O <sub>3</sub> %	Fe <sub>2</sub> O <sub>3</sub> %	K <sub>2</sub> O %
<b>light</b>																					
HLF17 1 III 14-15	1179.5	0.12	0.44	-28.6	43.8	0.91	0.16	11.2	75.7	13.2	3.6	17.3	56.7	2.9	9.2	0.8	59.0	0.4	2.7	1.8	1.1
HLF17 1 III 17-18	1182.5	0.12	0.52	-27.7	45.2	0.92	0.31	13.2	77.1	9.7	19.0	26.1	19.0	12.5	7.7	1.9	65.3	0.6	3.7	3.1	1.0
HLF 17 1 III 20-21	1185.5	0.10	0.48	-29.0	43.7	0.93	0.23	13.3	77.3	9.4	8.2	5.8	51.2	3.2	14.3	3.2	62.7	0.8	4.9	4.2	1.1
HLF17 1 III 33-34	1198.5	0.13	0.58	-28.1	40.1	0.90	0.22	11.3	78.6	10.1	5.3	11.3	45.2	10.7	12.9	0.0	64.4	0.7	4.3	3.6	1.1
HLF17 1 III 34.5-35	1200	0.16	0.66	-27.8	46.2	0.91	0.32	17.2	74.6	8.2	7.0	8.2	33.4	5.1	14.3	1.8	67.0	0.8	4.6	4.6	1.1
HLF 17 1 III 46-47	1211.5	0.12	0.48	-30.4	47.2	0.94	0.33	18.3	72.5	9.2	4.5	36.7	22.3	7.3	12.3	2.5	64.4	0.5	3.0	2.4	0.9
HLF 17 1 III 51-52	1216.5	0.10	0.58	-29.3	50.4	0.93	0.42	15.3	75.2	9.6	7.4	10.8	56.8	4.0	6.7	0.9	n.m.	n.m.	n.m.	n.m.	n.m.
HLF17 1 III 57-58	1222.5	0.11	0.45	-29.5	37.9	0.93	0.18	11.7	78.9	9.4	9.5	20.3	36.1	6.3	11.0	3.8	63.2	0.7	3.5	3.6	0.8
HLF 17 1 III 63-64	1228.5	0.14	0.63	-28.6	47.6	0.92	0.31	12.5	78.5	9.1	8.3	5.5	40.1	6.0	12.1	8.6	68.4	0.7	3.6	3.4	1.0
HLF17 1 III 71-72	1236.5	0.12	0.49	-29.9	45.1	0.94	0.21	13.4	77.9	8.7	9.4	16.8	45.3	2.8	9.3	2.2	66.4	0.4	2.3	1.9	0.7
HLF17 1 III 73.5-74.5	1239	0.13	0.60	-30.0	49.6	0.93	0.18	15.5	75.4	9.0	17.4	9.0	25.0	3.3	18.2	3.3	67.6	0.5	2.8	2.3	0.8
HLF17 1 III 80.5-81.5	1246	0.10	0.40	-29.3	30.2	0.92	0.20	13.2	75.0	11.7	1.3	44.6	24.2	2.1	10.5	7.8	60.6	0.8	4.5	3.9	1.1
HLF17 1 III 84.5-85.5	1250	0.11	0.56	-27.8	44.6	0.93	0.24	12.9	77.3	9.9	12.5	14.0	31.6	6.4	11.4	7.8	68.4	0.6	3.6	3.1	1.0
HLF 17 1 III 86.5-87.5	1252	0.10	0.51	-28.4	37.1	0.92	0.22	12.9	76.2	10.8	14.7	8.3	24.9	13.4	8.6	10.7	68.4	0.6	3.8	3.0	0.9
HLF17 1 III 91-92	1256.5	0.11	0.48	-28.2	34.1	0.91	0.42	12.9	74.7	12.3	10.5	18.6	35.8	1.9	9.6	1.2	63.2	0.9	5.0	4.2	1.2
	<b>mean</b>	<b>0.12</b>	<b>0.52</b>	<b>-28.8</b>	<b>42.9</b>	<b>0.92</b>	<b>0.26</b>	<b>13.6</b>	<b>76.3</b>	<b>10.0</b>	<b>9.2</b>	<b>16.9</b>	<b>36.5</b>	<b>5.9</b>	<b>11.2</b>	<b>3.8</b>	<b>64.9</b>	<b>0.6</b>	<b>3.7</b>	<b>3.2</b>	<b>1.0</b>
	<b>s.d.</b>	<b>0.02</b>	<b>0.08</b>	<b>0.9</b>	<b>5.8</b>	<b>0.01</b>	<b>0.08</b>	<b>2.1</b>	<b>1.8</b>	<b>1.4</b>	<b>5.0</b>	<b>11.4</b>	<b>12.4</b>	<b>3.7</b>	<b>3.0</b>	<b>3.3</b>	<b>3.0</b>	<b>0.2</b>	<b>0.8</b>	<b>0.9</b>	<b>0.1</b>
<b>dark</b>																					
HLF17 1 III 1-2	1166.5	0.14	0.73	-26.4	36.2	0.87	0.76	13.4	79.0	7.6	3.0	0.8	48.4	3.4	19.9	3.4	65.6	1.1	6.0	5.3	1.3
HLF17 1 III 3-4	1168.5	0.13	0.74	-26.8	34.7	0.89	0.42	14.6	77.5	8.0	8.0	1.0	41.6	3.9	18.4	4.6	64.8	0.9	5.2	4.7	1.3
HLF17 1 III 6-7	1171.5	0.13	0.69	-25.3	28.0	0.85	2.13	15.0	77.6	7.4	2.4	0.0	72.2	2.5	9.1	4.5	65.5	1.2	6.8	5.7	1.5
HLF17 1 III 11-12	1176.5	0.12	0.66	-25.9	30.4	0.89	0.57	11.2	79.4	9.4	4.9	6.4	46.0	4.5	23.0	1.5	65.6	0.8	4.5	3.9	1.2
HLF 17 1 III 16-17	1181.5	0.14	0.84	-27.0	35.3	0.90	0.80	13.8	77.8	8.4	3.9	3.6	51.3	2.2	22.4	1.4	67.3	0.8	4.7	4.5	1.2
HLF 17 1 III 18-19	1183.5	0.13	0.69	-27.1	37.4	0.89	0.31	17.2	75.3	7.5	5.2	1.3	39.0	27.2	9.0	5.4	66.1	0.8	4.8	4.3	1.2
HLF17 1 III 27-28	1192.5	0.14	0.78	-26.9	30.1	0.88	0.81	13.6	78.0	8.5	9.7	3.4	52.3	4.1	17.6	0.5	66.1	1.0	5.7	4.8	1.4
HLF17 1 III 39-40	1204.5	0.11	0.46	-28.0	27.0	0.91	0.43	12.2	76.2	11.6	4.7	9.3	18.9	40.4	3.7	1.9	64.2	1.0	5.7	4.9	1.3
HLF17 1 III 42.5-43.5	1208	0.12	0.60	-27.1	34.2	0.91	0.42	17.3	74.2	8.5	11.1	4.9	41.6	4.7	18.5	1.3	68.2	0.7	3.9	3.4	1.0
HLF17 1 III 43.5-44	1208.75	0.13	0.64	-27.3	36.3	0.92	0.29	14.1	76.3	9.6	4.3	19.2	27.9	1.0	17.8	1.3	65.3	0.8	4.1	3.7	1.1
HLF17 1 III 44.5-45	1209.75	0.10	0.51	-28.8	41.8	0.93	0.23	14.9	75.6	9.5	2.6	36.3	25.0	5.9	14.1	1.1	60.6	1.0	6.2	5.0	1.4
HLF17 1 III 48-49	1213.5	0.10	0.46	-28.1	30.2	0.92	0.36	13.1	77.8	9.1	4.2	15.7	26.6	9.9	19.3	1.5	64.5	0.7	4.1	4.0	0.9
HLF17 1 III 55-56	1220.5	0.13	0.68	-25.3	39.6	0.88	1.12	11.3	79.3	9.4	5.9	0.4	57.6	2.3	18.7	1.8	67.0	0.9	5.2	4.9	1.1
HLF17 1 III 60-61	1225.5	0.12	0.64	-26.4	35.8	0.88	0.83	14.6	76.8	8.7	3.8	1.9	53.7	5.0	15.1	2.6	63.5	1.1	6.0	5.6	1.4
HLF17 1 III 72.5-73.5	1238	0.12	0.56	-27.4	33.7	0.90	0.42	12.6	78.0	9.3	4.8	10.7	41.6	5.8	12.8	2.5	67.9	0.9	5.0	4.4	1.2
HLF 17 1 III 82.5-83	1247.75	0.11	0.57	-26.9	29.6	0.92	1.78	14.6	76.7	8.7	5.2	13.9	20.4	5.3	22.8	2.7	64.5	0.8	4.2	3.9	1.1
HLF17 1 III 83.5-84	1248.75	0.11	0.56	-28.6	45.3	0.93	0.30	17.7	73.0	9.3	17.6	22.2	16.0	4.4	18.7	2.0	63.9	0.7	3.8	3.6	0.9
HLF17 1 III 88.5-89.5	1254	0.12	0.64	-27.2	30.5	0.89	1.37	12.9	77.8	9.3	14.4	3.3	46.5	4.8	11.8	2.3	65.7	1.0	5.8	5.0	1.3
HLF17 1 III 95.5-96.5	1261	0.13	0.65	-25.9	34.0	0.87	2.50	13.2	77.8	9.0	4.1	3.8	49.3	3.5	18.1	3.5	66.3	1.0	6.2	5.3	1.3
	<b>mean</b>	<b>0.12</b>	<b>0.64</b>	<b>-27.0</b>	<b>34.2</b>	<b>0.89</b>	<b>0.83</b>	<b>14.1</b>	<b>77.0</b>	<b>8.9</b>	<b>6.3</b>	<b>8.3</b>	<b>40.8</b>	<b>7.4</b>	<b>16.4</b>	<b>2.4</b>	<b>65.4</b>	<b>0.9</b>	<b>5.2</b>	<b>4.6</b>	<b>1.2</b>
	<b>s.d.</b>	<b>0.01</b>	<b>0.10</b>	<b>1.0</b>	<b>4.7</b>	<b>0.02</b>	<b>0.66</b>	<b>1.8</b>	<b>1.7</b>	<b>1.0</b>	<b>4.1</b>	<b>9.5</b>	<b>14.9</b>	<b>9.7</b>	<b>5.2</b>	<b>1.3</b>	<b>1.8</b>	<b>0.1</b>	<b>0.9</b>	<b>0.7</b>	<b>0.2</b>
<b>T-test (<math>p &lt; 0.01</math>)</b>			*	*	*	*	*			*					*			*	*	*	*

n.m. = not measured.

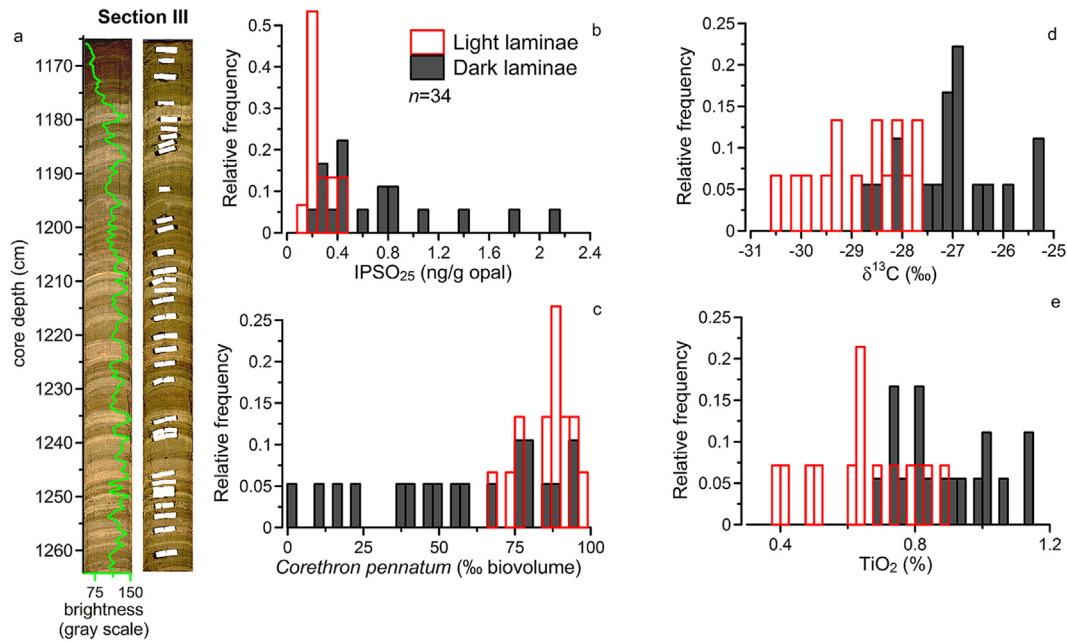


**Fig. 3.** Dark and light lamina analysis in section III. (a) Brightness (green line) and sub-sampled horizons ( $n = 34$ ); relative frequency of (b)  $\text{IPSO}_{25}$ , (c) *Corethron pennatum* (d)  $\delta^{13}\text{C}$  and (e)  $\text{TiO}_2$  in the light (red open bars) and dark (gray filled bars) laminae, respectively. (For interpretation of the references to colour in this figure legend, the reader is referred to the Web version of this article.)

lithogenic particle flux to sediments.

#### 4.2. Annual variability and lamination pattern

Overall, our collective biogenic and geochemical proxy data obtained from well-defined laminae suggest that fast ice evolution during summer in the Edisto inlet resulted in the deposition of laminae possessing different colour and composition. Further, by co-plotting the  $\text{IPSO}_{25}$ ,  $\delta^{13}\text{C}$  (OM) and *C. pennatum* (% biovolume) datasets (Fig. 4), the two proposed dominant fast ice patterns can be visualized and summarized as follows. At the beginning of summer, the progressive opening of the inlet takes place, leading to the accumulation of dark laminae characterized by high  $\text{IPSO}_{25}$ , enriched  $\delta^{13}\text{C}$  (OM) and low *C. pennatum* (% biovolume) (Fig. 4). We infer that the biogenic material that forms these darker laminae has two main sources: (i) sympagic diatoms living within the brine matrix of sea ice, which are subsequently released as the ice thaws, and (ii) diatoms that flourish in surface waters as the inlet opens in summer (e.g. *F. curta*). Further, since satellite images show that the complete opening of the inlet can take a few weeks, we believe that the deposition of sea ice diatoms and sea ice-associated diatoms likely co-exist. This is confirmed by the co-occurrence of  $\text{IPSO}_{25}$  and HBI III in the dark laminae (Fig. S3), the latter being derived from certain pelagic diatoms (e.g. Belt et al., 2017) and commonly found in marginal sea ice zones (Belt et al., 2015; Smik et al., 2016; Vorrath et al., 2019).

When protracted opening of the inlet occurs (i.e. ice free conditions), the surface nutrient limitation likely favours diatoms that can uptake nutrients underneath the pycnocline typical of oligotrophic waters which develop towards the end of the summer (Alley et al., 2018). Under these conditions, *C. pennatum* dominates, generating light laminae (Fig. 4), possibly in the form of rapidly sinking mats bound together by exopolymer mucus secretions and entangled spines (Alley et al., 2018). Our interpretation would clearly benefit from contemporary in situ studies dealing with the composition (diatoms, biomarkers, etc.) of seasonal sinking particulate material inside Antarctic inlets. To the best of our

knowledge, however, sediment traps have been deployed for this kind of setting only for short periods (Thomas et al., 2001), although longer studies in the Southern Ocean have been carried out primarily in deep- and mid-shelf environments (Smith et al., 2000).

Our general description of two discrete sea ice scenarios can be refined further by reference to satellite images of the inlet, which reveal marked inter-annual variability of fast ice conditions in summer. For example, Fig. 5 shows satellite images from three years (i.e. 2012, 2017, 2018) that clearly describe the full spectrum of proposed ice cover and its transitions. Thus, in 2017, ice break-up took place at the beginning of the summer, followed by protracted opening of the inlet. Under these conditions, we infer the deposition of both dark and light laminae (Fig. 5a). In contrast, in 2012, thawing of fast ice was delayed, and the inlet never completely opened by the end of the summer. In this scenario, it is likely that deposits were dominated by dark laminae due to only partial and ephemeral opening of the inlet (Fig. 5b). Finally, in 2018, fast ice persisted throughout the summer along the coastal region. We envision that these circumstances prevented the accumulation of biogenic material or, alternatively, resulted in only a thin deposit (i.e. condensed unit) (Fig. 5c).

Overall, satellite images from the Edisto inlet taken over the last decade suggest that fast ice dynamics during summer can sometimes be more complex than a simple sequential accumulation of dark and light laminae, as inferred for 2017. This is confirmed by the laminations pattern of HLF17-1 that does not exhibit recurring patterns at multi-year scale (i.e. over cm or dm) (Fig. 2), likely reflecting the dynamic annual variability in summer sea ice conditions revealed by satellite images shown herein from 2012, 2017 and 2018.

#### 4.3. Local reservoir effect and Bayesian age-depth model

Calibrations of radiocarbon ages obtained from carbon pools that are not in equilibrium with the atmosphere require a correction due to the influence of the reservoir effect (Stuiver and Polach,

1977). In addition to the global mean marine reservoir (R) modelled when using the Marine13 curve (Reimer et al., 2013), a further offset ( $\Delta R$ ) needs to be applied to accommodate local influences. Here, we built our age-depth model using  $^{14}\text{C}$  ages derived from both carbonate and organic carbon matrices, with additional dates obtained from excess  $^{210}\text{Pb}$  and one tephra horizon. Considering the mixed nature of the radiocarbon tests (i.e. organic and inorganic carbon), we used two different local reservoir corrections prior to calibration. Based on U/Th dating of coral samples trapped by the fringing Ross Sea ice shelf (Hall et al. 2010), the  $\Delta R$  value of the carbonate matrix ( $\Delta R_{\text{CaCO}_3}$ ) in the Ross Sea has remained relatively stable ( $\Delta R_{\text{CaCO}_3} = 791 \pm 121$  yrs) over the last 6000 years. In our records, carbonate tests included benthic foraminifera, planktonic foraminifera and Ophiuroidea found in core HLF16-1 (Table 1), and were correlated with core HLF17-1 using distinct lamination patterns common to both cores (Fig. S1, Supplementary Material). For consistency, only benthic foraminifera were used in the final age model, while additional carbonate samples (planktonic foraminifera and Ophiuroidea) from the same core depths were used to independently test the robustness of our chronology and assumptions behind using  $\Delta R_{\text{CaCO}_3}$  (Table 1). Following calibration, all carbonate skeletal elements belonging to the same horizon displayed similar calendar ages, confirming that the  $\Delta R_{\text{CaCO}_3}$ , in addition to being stable over the late-Holocene (Hall et al., 2010), is also appropriate for diverse calcifying organisms (Table 1).

In contrast, the  $\Delta R$  of the acid insoluble organic fraction ( $\Delta R_{\text{OC}}$ ) is poorly constrained in Antarctic sediments and is usually derived empirically by radiocarbon dating of surface bulk sediments and their interpolation (Domack et al., 2001; Licht et al., 1998; Mezgec et al., 2017). In the Edisto inlet, Mezgec et al. (2017) used core-top data (box-core BAY05-bc21, 0–1 cm) to propose a value of  $1580 \pm 45$  years as a general  $R_{\text{OC}}$  (global +  $\Delta R$ ). However, using the same approach, the remarkably young  $^{14}\text{C}$  age ( $200 \pm 30$  yrs BP; Table 1) of the surface sediment from box core HLF17-2BC (0–0.5 cm) collected at the same site as piston core HLF17-1, suggests that our core top likely contained “bomb”  $^{14}\text{C}$ , which prevents its use to assess  $\Delta R_{\text{OC}}$ .

Given the evident limitations of using surface sediments to estimate the local reservoir effect, we derived the  $\Delta R_{\text{OC}}$  by pairing benthic foraminifera (ultimately used in the age-depth model) with organic carbon from the same horizons, relying on the well-constrained  $\Delta R_{\text{CaCO}_3}$ . This alternative approach assumes that the accumulation of foraminifera and the deposition of organic carbon in the same horizons were coeval with negligible post-depositional transport. This allowed us to subtract the  $^{14}\text{C}$  age of foraminifera (adjusted for  $\Delta R_{\text{CaCO}_3}$ ) from the  $^{14}\text{C}$  age of the organic fraction to obtain the  $\Delta R_{\text{OC}}$  for each level and its relative uncertainty. The average of the three values gave an estimate of the final mean  $\Delta R_{\text{OC}}$  ( $1320 \pm 135$  yrs,  $1\sigma$ ). Additional dates used in the age-depth model include the maximum penetration of excess  $^{210}\text{Pb}$  ( $150 \pm 20$  yrs before 2017, Figs. S1 and S4; ca. seven half-lives according to Arias-Ortiz et al. (2018)) and a tephra layer recently found in the Edisto inlet sediments (Figs. S1 and S5) Mount Rittmann volcano eruption, (Di Roberto et al., 2019), which has been identified in the Talos Dome core ( $696 \pm 2$  yrs BP; ice record) (Narcisi et al., 2012), Taylor Dome core ( $709 \pm 71$  yrs BP; ice record) (Hawley et al., 2003) and West Antarctic Ice Sheet (WAIS) Divide cores ( $687 \pm 7$  yrs cal BP) (Di Roberto et al., 2019). For our final age-depth model, we used the more precise age assignment derived from the annually-counted portion of the WAIS Divide 2014 chronology.

Our final Bayesian age-depth model for HLF17-1 was built on seven dates (Table 1; Fig. 6). The age-depth model showed that, since 2.6 ka BP, the relatively stable and high accumulation rate in the inlet (ca. 0.7 cm/yr) was followed by an abrupt decrease around 0.7 ka BP (ca. 0.2 cm/yr) (Fig. 6).

#### 4.4. Late-Holocene reconstruction of sea-ice dynamics in the Edisto inlet

In order to reconstruct the fast ice dynamics during the late-Holocene, we analysed 295 sediment samples throughout piston core HLF17-1. Following our interpretation about the emplacement of laminated strata section III, we assumed that the down-core distribution of IPSO<sub>25</sub> and  $\delta^{13}\text{C}$  (OM) in bulk sediments co-varied as a function of the relative contribution of light and dark laminae. Since the two types of laminae could be further classified, statistically, into two distinct groups based on AHC and CT analyses (see Section 3), we identified suitable thresholds for IPSO<sub>25</sub> (0.42 ng/g opal) and  $\delta^{13}\text{C}$  ( $-27.56\text{‰}$ ) to best separate the laminae analysed in section III (Fig. 4) into light and dark groupings (Supplementary Material, Fig. S6). By applying these thresholds to bulk sediments, we obtained two sub-groups of IPSO<sub>25</sub> and  $\delta^{13}\text{C}$  (OM) which succinctly represented the two dominant types of fast ice coverage in summer: initial summer break-up and ice-free conditions (dashed lines in Fig. 7a and b). As described previously (Section 2), we expected that the third condition – inlet covered throughout the summer – would not be uniquely characterized in our laminated sequence. Rather, when this occurred, permanent fast ice probably resulted in either a gap in accumulation or a condensed sediment unit. Regardless of this limitation, comparison between the down-core sediment brightness and clustered IPSO<sub>25</sub> and  $\delta^{13}\text{C}$  (OM) bulk data revealed a good agreement, especially for IPSO<sub>25</sub> (Fig. 7a and b). This further confirmed that the correlation between sediment colour and geochemical signature observed in section III (laminae) holds throughout the record.

Thus, we propose use of the same IPSO<sub>25</sub> and  $\delta^{13}\text{C}$  thresholds (dashed lines Fig. 7a and b) to identify periods throughout the late Holocene when fast ice break-up followed by an ice-free inlet was more frequent (gray shaded areas) relative to periods characterized by partial opening of the inlet (see Fig. 5a and 5b, respectively). Using this approach, we identify a significant change in the relative frequency of inlet opening and ice-free waters during the late-Holocene. Specifically, our results suggest that between 2.6 ka BP and 0.7 ka BP the inlet opened regularly during summer, while after 0.7 ka BP, there was an abrupt shift characterized by relatively less frequent ice-free conditions (e.g. Fig. 7a and b). It is worth noting that following the shift in ice conditions at 0.7 ka BP, the sediment accumulation rate of the record decreased abruptly from 0.7 to 0.2 cm/yr. This likely occurred due to the absence (or lower frequency) of light laminae deposition, resulting in relatively thinner sediment strata over summers. Finally, the bulk grain-size exhibited a similar temporal shift, becoming progressively coarser after ca. 1.3 ka BP. This overall trend was expected based on the analysis of dark and light laminae, which also displayed small, but statistically significant differences (Table 2;  $p < 0.01$ ), although the reason why dark laminae were coarser is, as yet, unknown. We speculate that this might be attributable to the relatively higher concentration of lithogenic material in the dark laminae mode of dust ranges between 76 and 129  $\mu\text{m}$ , (Atkins and Dunbar, 2009). Nevertheless, the difference between light and dark laminae is somehow counterintuitive considering that the former are dominated by *C. pennatum*, which, as described before, is considerably larger than other diatoms more abundant in dark laminae. However, since *C. pennatum* was mostly present as fragments, despite its high abundance, it is possible that lithic particles played a major role in the overall grain-size distribution.

#### 4.5. Fast ice dynamics over the late-Holocene and climate forcing

In order to understand the origin of the shift in sea ice conditions observed around 0.7 ka BP, we compared our results with the

**Table 3**  
Relative abundance of diatoms in dark and light laminae as counts and biovolume.

laminae	depth (cm)		<i>Chaetoceros</i>	<i>Chaetoceros</i>	<i>Corethron</i>	<i>Eucampia</i>	<i>Fragilariopsis</i>	<i>Fragilariopsis</i>	<i>Fragilariopsis</i>	<i>Rhizosolenia</i>	total
			RS	<i>dichaeta</i>	<i>pennatum</i>	<i>antarctica</i>	<i>curta</i>	<i>cylindrus</i>	<i>obliquocostata</i>	spp.	
			relative abundance (counts), %								
<b>light</b>											
HLF17 1 III 14-15	1179.5	Light	3.6	0.0	17.3	0.0	56.7	2.9	9.2	0.3	90.0
HLF17 1 III 17-18	1182.5	Light	19.0	0.0	26.1	0.0	19.0	12.5	7.7	0.3	84.5
HLF 17 1 III 20-21	1185.5	Light	8.2	0.9	5.8	0.0	51.2	3.2	14.3	0.0	83.5
HLF17 1 III 33-34	1198.5	Light	5.3	0.0	11.3	0.0	45.2	10.7	12.9	0.3	85.6
HLF17 1 III 34.5-35	1200	Light	7.0	1.0	8.2	0.3	33.4	5.1	14.3	0.5	69.9
HLF 17 1 III 46-47	1211.5	Light	4.5	0.0	36.7	0.0	22.3	7.3	12.3	0.6	83.8
HLF 17 1 III 51-52	1216.5	Light	7.4	0.8	10.8	0.0	56.8	4.0	6.7	0.0	86.6
HLF17 1 III 57-58	1222.5	Light	9.5	0.0	20.3	0.0	36.1	6.3	11.0	0.3	83.6
HLF 17 1 III 63-64	1228.5	Light	8.3	4.3	5.5	0.2	40.1	6.0	12.1	0.0	76.3
HLF17 1 III 71-72	1236.5	Light	9.4	0.3	16.8	0.1	45.3	2.8	9.3	0.0	84.0
HLF17 1 III 73.5-74.5	1239	Light	17.4	0.0	9.0	0.2	25.0	3.3	18.2	0.0	73.1
HLF17 1 III 80.5-81.5	1246	Light	1.3	0.0	44.6	0.0	24.2	2.1	10.5	0.0	82.7
HLF17 1 III 84.5-85.5	1250	Light	12.5	2.5	14.0	0.0	31.6	6.4	11.4	0.0	78.3
HLF 17 1 III 86.5-87.5	1252	Light	14.7	0.3	8.3	0.0	24.9	13.4	8.6	0.7	70.8
HLF17 1 III 91-92	1256.5	Light	10.5	1.9	18.6	0.0	35.8	1.9	9.6	0.3	78.6
			<b>average</b>	<b>9.2</b>	<b>0.8</b>	<b>16.9</b>	<b>0.0</b>	<b>36.5</b>	<b>5.9</b>	<b>11.2</b>	<b>0.2</b>
			<b>s.d.</b>	<b>5.0</b>	<b>1.2</b>	<b>11.4</b>	<b>0.1</b>	<b>12.4</b>	<b>3.7</b>	<b>3.0</b>	<b>0.2</b>
<b>dark</b>											
HLF17 1 III 1-2	1166.5	Dark	3.0	7.7	0.8	0.0	48.4	3.4	19.9	0.0	83.2
HLF17 1 III 3-4	1168.5	Dark	8.0	2.6	1.0	0.0	41.6	3.9	18.4	0.4	75.9
HLF17 1 III 6-7	1171.5	Dark	2.4	1.8	0.0	0.0	72.2	2.5	9.1	0.0	87.9
HLF17 1 III 11-12	1176.5	Dark	4.9	0.0	6.4	0.0	46.0	4.5	23.0	0.0	84.7
HLF 17 1 III 16-17	1181.5	Dark	3.9	0.9	3.6	0.0	51.3	2.2	22.4	0.5	84.8
HLF 17 1 III 18-19	1183.5	Dark	5.2	1.6	1.3	0.0	39.0	27.2	9.0	0.2	83.6
HLF17 1 III 27-28	1192.5	Dark	9.7	2.1	3.4	0.0	52.3	4.1	17.6	0.0	89.2
HLF17 1 III 39-40	1204.5	Dark	4.7	0.5	9.3	0.1	18.9	40.4	3.7	0.3	77.9
HLF17 1 III 42.5-43.5	1208	Dark	11.1	0.2	4.9	0.3	41.6	4.7	18.5	0.2	81.5
HLF17 1 III 43.5-44	1208.8	Dark	4.3	0.3	19.2	0.1	27.9	1.0	17.8	0.3	70.9
HLF17 1 III 44.5-45	1209.8	Dark	2.6	0.0	36.3	0.6	25.0	5.9	14.1	0.0	84.5
HLF17 1 III 48-49	1213.5	Dark	4.2	1.7	15.7	1.7	26.6	9.9	19.3	0.3	79.3
HLF17 1 III 55-56	1220.5	Dark	5.9	1.4	0.4	0.0	57.6	2.3	18.7	0.5	86.9
HLF17 1 III 60-61	1225.5	Dark	3.8	5.0	1.9	0.0	53.7	5.0	15.1	0.0	84.6
HLF17 1 III 72.5-73.5	1238	Dark	4.8	2.2	10.7	1.1	41.6	5.8	12.8	0.3	79.2
HLF 17 1 III 82.5-83	1247.8	Dark	5.2	0.5	13.9	0.8	20.4	5.3	22.8	0.5	69.4
HLF17 1 III 83.5-84	1248.8	Dark	17.6	0.4	22.2	0.0	16.0	4.4	18.7	0.0	79.3
HLF17 1 III 88.5-89.5	1254	Dark	14.4	1.0	3.3	0.0	46.5	4.8	11.8	0.5	82.3
HLF17 1 III 95.5-96.5	1261	Dark	4.1	3.5	3.8	0.3	49.3	3.5	18.1	0.6	83.3
			<b>average</b>	<b>6.3</b>	<b>1.8</b>	<b>8.3</b>	<b>0.3</b>	<b>40.8</b>	<b>7.4</b>	<b>16.4</b>	<b>0.2</b>
			<b>s.d.</b>	<b>4.1</b>	<b>1.9</b>	<b>9.5</b>	<b>0.5</b>	<b>14.9</b>	<b>9.7</b>	<b>5.2</b>	<b>0.2</b>
<b>T-test (p&lt;0.05)</b>					*						
<b>T-test (p&lt;0.01)</b>					*						

<sup>a</sup> Percent biovolume = 100 \* (% relative abundance \* V avg)/Total biovolume (from Alley et al., 2018).

<sup>b</sup> Average biovolume from Alley et al. (2018).

extensive dataset compiled by Stenni et al. (2017) within the umbrella of the PAGES Antarctica2k programme. The entire database consists of water stable isotope data ( $\delta^{18}\text{O}$  and  $\delta\text{D}$ ) from 112 records, which permitted a high-resolution reconstruction of past temperature and relative anomalies (relative to 1900–1990 CE) over the last 2 ka BP for seven climatically distinct regions of Antarctica. The composite temperature anomalies reconstruction (10-yr-binned averages; Fig. 7d) for the Victoria Land Coast region based on ice cores near to HLF17-1 (Fig. 1a) shows a clear and abrupt cooling at 0.7 ka BP, which follows the general long-term cooling over Antarctica that started at ca 1.2 ka BP. Previously, Stenni et al. (2017) argued that this hemispheric-scale cooling could have been driven by major volcanic eruptions, in agreement with previous studies (McGregor et al., 2015). Although the cause of this cooling over the last two millennia is beyond the scope of the

current study, it is worth noting that the land fast ice reconstruction based on our marine record agrees well with the temperature anomalies recorded in the Victoria Land Coast. Thus, we attribute less frequent ice-free conditions since 0.7 ka BP to a colder climate inferred from ice core data (Stenni et al., 2017), although we also note that our marine record resolves summer dynamics only, while ice cores provide a year-round signature.

We also compared our results with those of Mezgec et al. (2017) who analysed Holocene diatom assemblages in cores taken from Cape Hallett and Wood Bay (Ross Sea). Interestingly, their data show a sharp increase in the relative concentration of *F. curta* during the late Holocene, which is consistent with the occurrence of more frequent dark laminae in the current study (Tables 2 and 3), thus supporting our interpretation of less protracted opening of the inlet during summers along the coast.

	<i>Chaetoceros</i> RS	<i>Chaetoceros</i> <i>dichaeta</i>	<i>Corethron</i> <i>pennatum</i>	<i>Eucampia</i> <i>antarctica</i>	<i>Fragilariopsis</i> <i>curta</i>	<i>Fragilariopsis</i> <i>cylindrus</i>	<i>Fragilariopsis</i> <i>obliquecostata</i>	<i>Rhizosolenia</i> spp.
	<b>relative abundance (biovolume), %<sup>a</sup></b>							
average biovolume ( $\mu\text{m}^3$ ) <sup>b</sup>	277	19227	70686	40457	642	231	4936	169222
<b>light</b>	0.1	0.0	89.8	0.0	2.7	0.0	3.3	4.0
	0.3	0.0	94.7	0.0	0.6	0.1	2.0	2.2
	0.4	3.1	77.0	0.0	6.1	0.1	13.2	0.0
	0.2	0.0	84.4	0.0	3.1	0.3	6.7	5.3
	0.2	2.5	73.1	1.3	2.7	0.1	8.9	11.1
	0.0	0.0	93.5	0.0	0.5	0.1	2.2	3.7
	0.2	1.8	89.6	0.0	4.3	0.1	3.9	0.0
	0.2	0.0	91.6	0.0	1.5	0.1	3.5	3.2
	0.4	14.5	68.7	1.1	4.5	0.2	10.5	0.0
	0.2	0.4	93.0	0.5	2.3	0.1	3.6	0.0
	0.6	0.0	84.2	0.9	2.1	0.1	12.0	0.0
	0.0	0.0	97.9	0.0	0.5	0.0	1.6	0.0
	0.3	4.3	88.4	0.0	1.8	0.1	5.0	0.0
	0.5	0.8	76.1	0.0	2.1	0.4	5.5	14.6
	0.2	2.4	89.0	0.0	1.6	0.0	3.2	3.6
	<b>0.3</b>	<b>2.0</b>	<b>86.1</b>	<b>0.3</b>	<b>2.4</b>	<b>0.1</b>	<b>5.7</b>	<b>3.2</b>
	<b>0.2</b>	<b>3.7</b>	<b>8.7</b>	<b>0.5</b>	<b>1.6</b>	<b>0.1</b>	<b>3.8</b>	<b>4.4</b>
<b>dark</b>	0.2	43.8	17.6	0.0	9.2	0.2	29.0	0.0
	0.7	15.9	21.9	0.0	8.6	0.3	29.4	23.3
	0.5	27.1	0.0	0.0	36.6	0.5	35.4	0.0
	0.2	0.0	75.5	0.0	5.0	0.2	19.1	0.0
	0.2	3.3	50.7	0.0	6.6	0.1	22.2	16.8
	0.6	13.2	38.0	0.0	10.4	2.6	18.6	16.6
	0.7	10.0	59.5	0.0	8.3	0.2	21.4	0.0
	0.2	1.4	86.4	0.7	1.6	1.2	2.4	6.1
	0.6	0.7	67.5	2.1	5.2	0.2	17.8	5.9
	0.1	0.3	89.5	0.3	1.2	0.0	5.8	2.8
	0.0	0.0	95.8	1.0	0.6	0.1	2.6	0.0
	0.1	2.3	80.9	4.9	1.2	0.2	6.9	3.4
	0.6	9.8	11.2	0.0	13.2	0.2	32.8	32.3
	0.3	28.1	39.4	0.0	10.1	0.3	21.8	0.0
	0.1	4.4	76.7	4.6	2.7	0.1	6.4	4.8
	0.1	0.8	79.2	2.5	1.1	0.1	9.1	7.1
	0.3	0.5	93.1	0.0	0.6	0.1	5.5	0.0
	0.9	4.5	54.0	0.0	6.9	0.3	13.5	19.9
	0.2	11.6	46.5	2.2	5.5	0.1	15.4	18.5
	<b>0.4</b>	<b>9.3</b>	<b>57.0</b>	<b>1.0</b>	<b>7.1</b>	<b>0.4</b>	<b>16.6</b>	<b>8.3</b>
	<b>0.3</b>	<b>12.0</b>	<b>29.4</b>	<b>1.6</b>	<b>8.1</b>	<b>0.6</b>	<b>10.3</b>	<b>9.8</b>
		*			*		*	*

Another important factor that can have large-scale implications for fast-ice dynamics over Antarctica is the non-annular response (i.e. dipole) of the Southern Ocean to the Southern Annular Mode (SAM) (Bertler et al., 2018; Lefebvre and Gooose, 2005; Lefebvre et al., 2004). This dipole consists of a different regional response in sea ice, with decreases in the Weddell Sea and around the Antarctic Peninsula, and an increase in the Ross and Amundsen Seas during years with a positive SAM index. Due to a low-pressure anomaly in the Amundsen-Bellingshausen sector during positive SAM years, the Weddell and Bellingshausen Seas are subject to more northerly winds, while the Ross Sea tends to have more southerly winds (Lefebvre et al., 2004), inducing a significant cooling at the surface and an increase in the Ross Sea ice cover (Lefebvre and Gooose, 2005; Lefebvre et al., 2004). However, as far as our data are concerned, comparison between our reconstructed fast ice dynamics and the SAM derived from proxy records over the last 1000 yrs (Fig. 7e) (Abram et al., 2014) does not suggest a direct influence of the latter. In particular, the abrupt shift that

characterizes our record around 0.7 ka BP even opposes that expected from a negative SAM (Lefebvre et al., 2004). Likewise, the negative SAM should also have resulted in warmer conditions over the Ross Sea, which does not concur with the sharp cooling reconstructed in the Victoria Land Coast region based on ice core records (Stenni et al., 2017) (Fig. 7d).

However, stronger westerlies in the region of the Antarctic Circumpolar Current during positive SAM induce an intensified eastward surface ocean current and, as a result of Ekman drift, a stronger northward surface current south of 45°S. This promotes upwelling over the margin of the Modified Circumpolar Deep Water, whose characteristics – warm and salty – can promote sea ice thawing in the Ross Sea despite the general wind-driven surface cooling (Lefebvre and Gooose, 2005; Lefebvre et al., 2004). Thus, the negative SAM during the late-Holocene might have reduced the upwelling with direct effects on fast ice thawing. However, considering the small age uncertainties around the tephra layer (687 ± 7 yrs BP), the shift in our record almost certainly occurred

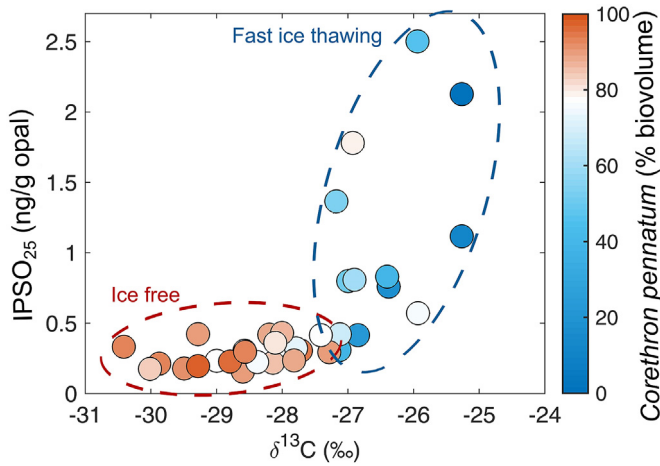


**Fig. 4.** Composition of laminae sub-sampled in (Section III) Blue and red dashed lines display the two dominant clusters which reflect contrasting sea ice coverages, namely fast ice thawing and ice-free conditions, respectively. (For interpretation of the references to colour in this figure legend, the reader is referred to the Web version of this article.)

before the change in the SAM index. Therefore, the role of upwelling on fast ice dynamics remains somewhat elusive, although a negative SAM after 0.7 ka presumably contributed to some preservation of coastal sea ice throughout the summer. Overall, we believe that the abrupt atmospheric cooling recorded over the Victoria Land Coast region (Stenni et al., 2017) likely exerted first-order control on the rapid shift of fast ice coverage in the inner Ross Sea during the late-Holocene, but other factors are more challenging to identify at this stage, in part, owing to the complex behaviour of sea ice cover, more generally (Meehl et al., 2019).

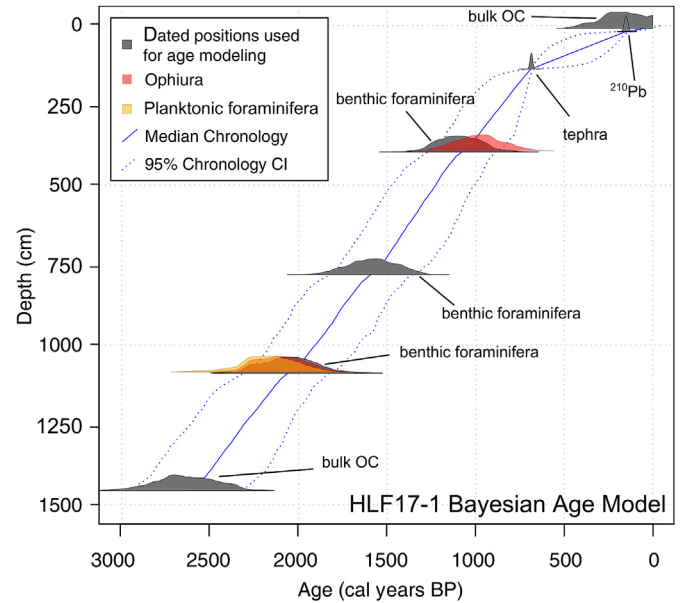


**Fig. 6.** Median calendar age (years before present) and  $2\sigma$  error from the Bayesian age-depth model of core HLF17-1. Gray colors show the dates used in the model. Additional carbonate dates (ophiurids and planktonic foraminifera) were used to test, independently, the age-model and the assumption behind the local marine reservoir age of the carbonate fraction. (For interpretation of the references to colour in this figure legend, the reader is referred to the Web version of this article.)

## 5. Conclusions

This study provides the first high-resolution late-Holocene reconstruction of fast ice dynamics in the Ross Sea (Edisto inlet)

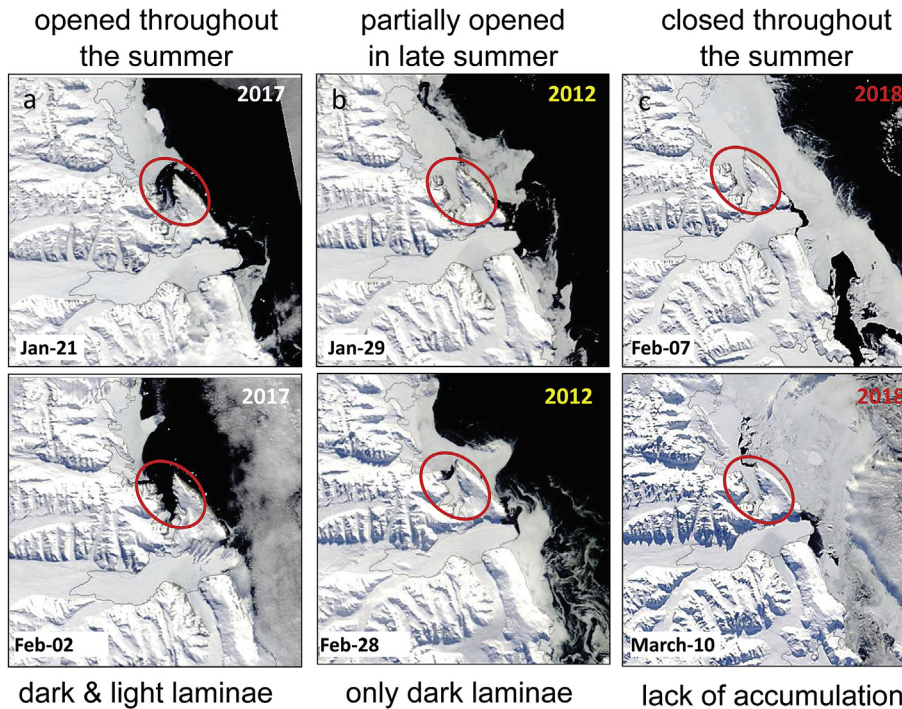


**Fig. 5.** Satellite images (a, 2017; b, 2012; c, 2018) of Edisto inlet (red ellipse) which provide the spectrum of sea ice coverage which, in turn, exerts first-order control on the formation of laminated sediments. 2017 was characterized by an early opening followed by protracted ice free conditions of the inlet. In 2012, thawing was incomplete and occurred toward the end of the summer. Finally, 2018 represented the end of the spectrum as sea ice persisted throughout the summer in the inlet. (For interpretation of the references to colour in this figure legend, the reader is referred to the Web version of this article.)

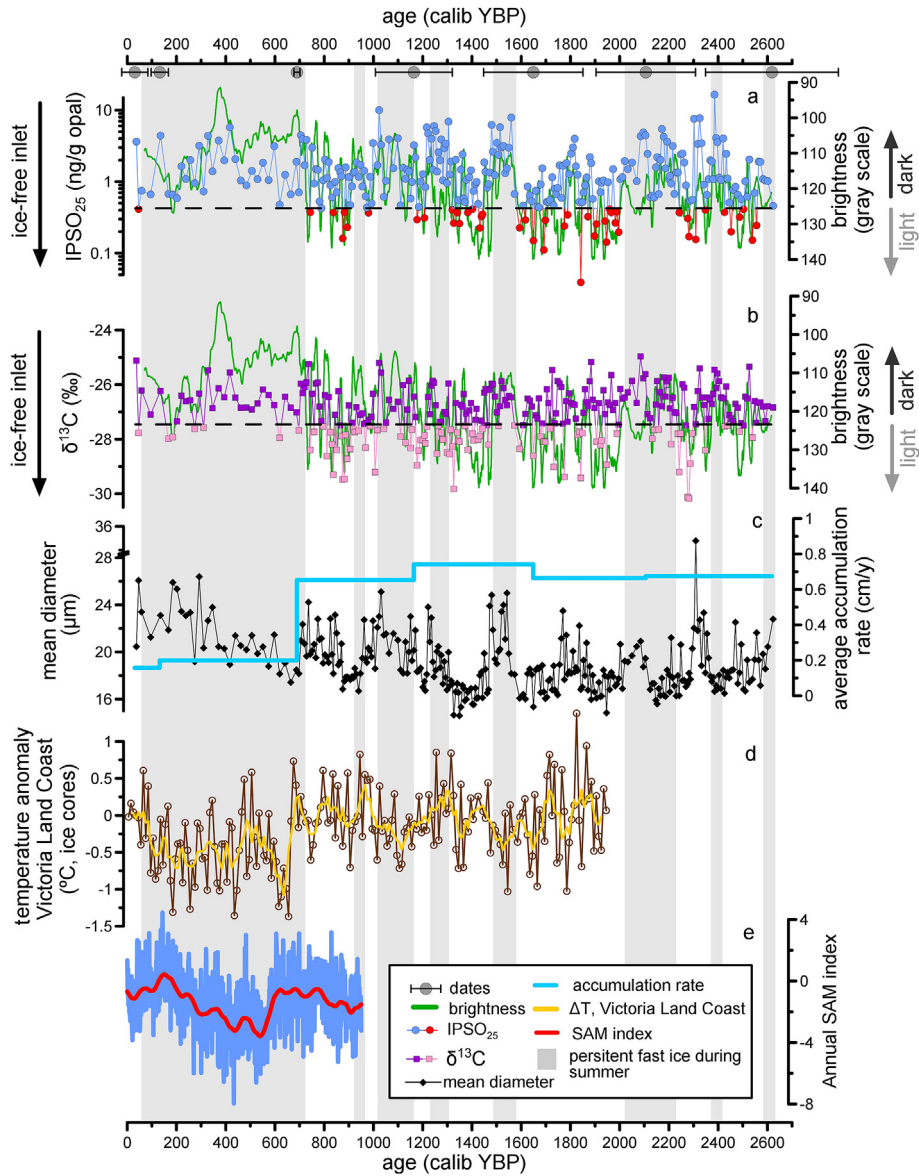


**Fig. 7.** Fast ice dynamics in the Edisto inlet and general climate conditions over the late-Holocene. Top filled blue circles show the dated horizons used in the age-depth model (a) IPSO<sub>25</sub> and brightness (11-point weighted average to match the IPSO<sub>25</sub> resolution), red and blue filled circles were defined according to the cluster analysis (see text for further details); (b)  $\delta^{13}\text{C}$  and brightness (11-point weighted average to match the IPSO<sub>25</sub> resolution), purple and pink filled squares were defined according to the cluster analysis (see text for further details); (c) sediment accumulation rate and grain-size; (d) 10-yr-binned averages of temperature anomalies in the ice cores (relative to 1900–1990 CE) (brown symbols) from the Victoria Land Coast ice cores (see Fig. 1a) and 5-point weight average (yellow line) (Stenni et al., 2017); (e) Reconstruction of annual Southern Annular Mode index (7-yr-binned average, blue line and 70-yr loess filter, red line) (Abram et al., 2014). Gray boxes define period characterized by regular opening of the inlet over summer (e.g. Fig. 5a). (For interpretation of the references to colour in this figure legend, the reader is referred to the Web version of this article.)

based on multiple proxies (IPSO<sub>25</sub>, diatom census counts and bulk properties) analysed in a 14.6 m long laminated diatom ooze record (HLF17-1). Our results indicate that the emplacement of laminated strata in the Edisto inlet reflect different fast ice cover during the summer months. In early summer, fast ice break-up releases sympagic diatoms living within the ice and platelet ice beneath. As the inlet opens, algal blooms in melt ponds promote sinking of phytodetritus, which accumulates with the sympagic diatoms. Overall, the opening of the inlet generates dark laminae characterized by relatively high concentrations of the sympagic biomarker IPSO<sub>25</sub>, high lithogenic material and enriched  $\delta^{13}\text{C}$  (OM) with a relatively heterogeneous distribution of diatoms. In late summer, when ice-free conditions persist, the diatom *Corethron pennatum* can adapt to stratified and oligotrophic waters, becoming the dominant

species and generating thick mats at the seabed. The resulting composition of light laminae is characterized by low IPSO<sub>25</sub> concentrations, low lithogenic material, and depleted  $\delta^{13}\text{C}$  (OM).

Building on the knowledge gained at lamina level, our down-core results show an abrupt change in summer fast ice dynamics over the late-Holocene. In particular, while the inlet appears to have opened regularly during summers since 2.6 ka BP, light laminae became suddenly less frequent around 0.7 ka BP, indicating an abrupt shift towards less recurrent ice-free conditions in the inlet. Comparison with ice core data from the region revealed that the abrupt shift in fast ice dynamics was likely the expression of colder climate conditions. Our results, both at seasonal (laminae) and late-Holocene scales, provide new insights into the application of the newly established IPSO<sub>25</sub> sea ice proxy, and in particular its

usefulness for paleo reconstructions of summer fast ice dynamics.

### Declaration of competing interest

The authors declare that they have no known competing financial interests or personal relationships that could have appeared to influence the work reported in this paper.

### CRediT authorship contribution statement

**T. Tesi:** Conceptualization, Methodology, Investigation, Writing - original draft, Writing - review & editing, Conceptualization. **S.T. Belt:** Writing - original draft, Writing - review & editing, Conceptualization. **K. Gariboldi:** Writing - original draft, Investigation, Data curation. **F. Muschitiello:** Writing - original draft, Formal analysis, Software. **L. Smik:** Writing - original draft, Investigation, Data curation. **F. Finocchiaro:** Writing - original draft, Investigation, Data curation. **F. Giglio:** Writing - original draft, Investigation, Data curation. **E. Colizza:** Writing - original draft, Investigation, Data curation. **G. Gazzurra:** Writing - original draft, Investigation, Data curation. **P. Giordano:** Writing - original draft, Investigation, Data curation. **C. Morigi:** Writing - original draft, Investigation. **L. Capotondi:** Writing - original draft, Investigation. **A. Nogarotto:** Writing - original draft, Investigation, Data curation. **D. Köseoglu:** Writing - original draft, Formal analysis, Software. **A. Di Roberto:** Writing - original draft, Investigation, Data curation. **A. Gallerani:** Investigation, Data curation. **L. Langone:** Writing - original draft, Investigation, Funding acquisition, Project administration.

### Acknowledgments

We thank the crew of the *R/V Italica* for their assistance during cruises. T.T. acknowledges funding from the CARISBO foundation (2017/0334). L.L. acknowledges funding from the Programma Nazionale Ricerche in Antartide – PNRA (PEA2013/AN2.03\_HOLO-FERNE). We thank Massimo Plessi, Antonella Gandolfi and Fabio Savelli for their assistance in the lab. All data from the current study can be found in the Supplementary Material. Finally, we thank two anonymous reviewers for providing supportive and useful feedback on the original manuscript.

### Appendix A. Supplementary data

Supplementary data to this article can be found online at <https://doi.org/10.1016/j.quascirev.2020.106299>.

### References

Abram, N.J., Mulvaney, R., Vimeux, F., Phipps, S.J., Turner, J., England, M.H., 2014. Evolution of the southern annular mode during the past millennium. *Nat. Clim. Change* 4, 564.

Alley, K., Patacka, K., Pike, J., Dunbar, R., Leventer, A., 2018. Iceberg Alley, East Antarctic margin: continuously laminated diatomaceous sediments from the late Holocene. *Mar. Micropaleontol.* 140, 56–68.

Arias-Ortiz, A., Masqué, P., García-Orellana, J., Serrano, O., Mazarrasa, I., Marbà, N., Lovelock, C.E., Lavery, P.S., Duarte, C.M., 2018. Reviews and Syntheses: 210 Pb-Derived Sediment and Carbon Accumulation Rates in Vegetated Coastal Ecosystems—Setting the Record Straight.

Armand, L., 1997. The Use of Diatom Transfer Functions in Estimating Sea-Surface Temperature and Sea-Ice in Cores from the Southeast Indian Ocean.

Armand, L.K., Crosta, X., Romero, O., Pichon, J.-J., 2005. The biogeography of major diatom taxa in Southern Ocean sediments: 1. Sea ice related species. *Palaeogeogr. Palaeoclimatol. Palaeoecol.* 223, 93–126.

Arrigo, K.R., DiTullio, G.R., Dunbar, R.B., Robinson, D.H., VanWoert, M., Worthen, D.L., Lizotte, M.P., 2000. Phytoplankton taxonomic variability in nutrient utilization and primary production in the Ross Sea. *J. Geophys. Res.: Oceans* 105, 8827–8846.

Arrigo, K.R., van Dijken, G.L., 2004. Annual changes in sea-ice, chlorophyll a, and primary production in the Ross Sea, Antarctica. *Deep Sea Res. Part II Top. Stud. Oceanogr.* 51, 117–138.

Atkins, C., Dunbar, G., 2009. Aeolian sediment flux from sea ice into Southern McMurdo Sound, Antarctica. *Global Planet. Change* 69, 133–141.

Bahk, J.J., Yoon, H.I., Kim, Y., Kang, C.Y., Bae, S.H., 2003. Microfabric analysis of laminated diatom ooze (Holocene) from the eastern Bransfield strait, Antarctic Peninsula. *Geosci. J.* 7, 135–142.

Belt, S., Smik, L., Brown, T., Kim, J.-H., Rowland, S., Allen, C., Gal, J.-K., Shin, K.-H., Lee, J., Taylor, K., 2016. Source identification and distribution reveals the potential of the geochemical Antarctic sea ice proxy IPSO<sub>25</sub>. *Nat. Commun.* 7, 12655.

Belt, S.T., November 2018. Source-specific biomarkers as proxies for Arctic and Antarctic sea ice. *Org. Geochem.* 125, 277–298.

Belt, S.T., 2019. What do IP<sub>25</sub> and related biomarkers really reveal about sea ice change? *Quat. Sci. Rev.* 204, 216–219.

Belt, S.T., Brown, T.A., Rodriguez, A.N., Sanz, P.C., Tonkin, A., Ingle, R., 2012. A reproducible method for the extraction, identification and quantification of the Arctic sea ice proxy IP<sub>25</sub> from marine sediments. *Anal. Meth.* 4, 705–713.

Belt, S.T., Brown, T.A., Smik, L., Tatarek, A., Wiktor, J., Stowasser, G., Assmy, P., Allen, C.S., Husum, K., 2017. Identification of C<sub>25</sub> highly branched isoprenoid (HBI) alkenes in diatoms of the genus *Rhizosolenia* in polar and sub-polar marine phytoplankton. *Org. Geochem.* 110, 65–72.

Belt, S.T., Cabedo-Sanz, P., Smik, L., Navarro-Rodriguez, A., Berben, S.M., Knies, J., Husum, K., 2015. Identification of paleo Arctic winter sea ice limits and the marginal ice zone: optimised biomarker-based reconstructions of late Quaternary Arctic sea ice. *Earth Planet Sci. Lett.* 431, 127–139.

Belt, S.T., Müller, J., 2013. The Arctic sea ice biomarker IP<sub>25</sub>: a review of current understanding, recommendations for future research and applications in palaeo sea ice reconstructions. *Quat. Sci. Rev.* 79, 9–25.

Belt, S.T., Smik, L., Köseoglu, D., Knies, J., Husum, K., 2019. A novel biomarker-based proxy for the spring phytoplankton bloom in Arctic and sub-arctic settings – HBI T<sub>25</sub>. *Earth Planet Sci. Lett.* 523, 115703.

Bertler, N.A., Conway, H., Dahl-Jensen, D., Emanuelsson, D.B., Winstrup, M., Vallengaard, P.T., Lee, J.E., Brook, E.J., Severinghaus, J.P., Fudge, T.J., 2018. The Ross Sea Dipole-temperature, snow accumulation and sea ice variability in the Ross Sea region, Antarctica, over the past 2700 years. *Clim. Past* 14, 193–214.

Bintanja, R., Van Oldenborgh, G., Drijfhout, S., Wouters, B., Katsman, C., 2013. Important role for ocean warming and increased ice-shelf melt in Antarctic sea-ice expansion. *Nat. Geosci.* 6, 376.

Collins, L.G., Allen, C.S., Pike, J., Hodgson, D.A., Weckström, K., Massé, G., 2013. Evaluating highly branched isoprenoid (HBI) biomarkers as a novel Antarctic sea-ice proxy in deep ocean glacial age sediments. *Quat. Sci. Rev.* 79, 87–98.

Crosta, X., Crespin, J., Billy, I., Ther, O., 2005. Major factors controlling Holocene δ<sup>13</sup>C<sub>org</sub> changes in a seasonal sea-ice environment, Adélie Land, East Antarctica. *Global Biogeochem. Cycles* 19.

Crosta, X., Koç, N., 2007. Chapter eight diatoms: from Micropaleontology to isotope geochemistry. In: Hillaire-Marcel, C., De Vernal, A. (Eds.), *Developments in Marine Geology*. Elsevier, pp. 327–369.

D'Angelo, A., Giglio, F., Miserocchi, S., Sanchez-Vidal, A., Aliani, S., Tesi, T., Viola, A., Mazzola, M., Langone, L., 2018. Multi-year particle fluxes in Kongsfjorden, Svalbard. *Biogeosci.* 15, 5343–5363.

Denis, D., Crosta, X., Barbara, L., Massé, G., Renssen, H., Ther, O., Giraudeau, J., 2010. Sea ice and wind variability during the Holocene in East Antarctica: insight on middle–high latitude coupling. *Quat. Sci. Rev.* 29, 3709–3719.

Denis, D., Crosta, X., Zaragosi, S., Romero, O., Martin, B., Mas, V., 2006. Seasonal and subseasonal climate changes recorded in laminated diatom ooze sediments, Adélie Land, East Antarctica. *Holocene* 16, 1137–1147.

Di Roberto, A., Colizza, E., Del Carlo, P., Petrelli, M., Finocchiaro, F., Kuhn, G., 2019. First marine cryptotephra in Antarctica found in sediments of the western Ross Sea correlates with englacial tephra and climate records. *Sci. Rep.* 9, 10628.

Dinelli, E., Lucchini, F., Fabbri, M., Corтеcci, G., 2001. Metal distribution and environmental problems related to sulfide oxidation in the Libiola copper mine area (Ligurian Apennines, Italy). *J. Geochem. Explor.* 74, 141–152.

Domack, E., Leventer, A., Dunbar, R., Taylor, F., Brachfeld, S., Sjunneskog, C., 2001. Chronology of the palmer deep site, Antarctic Peninsula: a Holocene palaeoenvironmental reference for the circum-Antarctic. *Holocene* 11, 1–9.

Etourneau, J., Collins, L.G., Willmott, V., Kim, J.H., Barbara, L., Leventer, A., Schouten, S., Sinninghe Damsté, J.S., Bianchini, A., Klein, V., Crosta, X., Massé, G., 2013. Holocene climate variations in the western Antarctic Peninsula: evidence for sea ice extent predominantly controlled by changes in insolation and ENSO variability. *Clim. Past* 9, 1431–1446.

Finocchiaro, F., Langone, L., Colizza, E., Fontolan, G., Giglio, F., Tuzzi, E., 2005. Record of the early Holocene warming in a laminated sediment core from Cape Hallett Bay (northern Victoria land, Antarctica). *Global Planet. Change* 45, 193–206.

Frignani, M., Langone, L., Ravaioli, M., Sorgente, D., Alvisi, F., Albertazzi, S., 2005. Fine-sediment mass balance in the western Adriatic continental shelf over a century time scale. *Mar. Geol.* 222, 113–133.

Geilfus, N.-X., Tison, J.-L., Ackley, S., Galley, R., Rysgaard, S., Miller, L., Delille, B., 2014. sea ice pCO<sub>2</sub> dynamics and air–ice CO<sub>2</sub> fluxes during the sea ice mass balance in the Antarctic (SIMBA) experiment—Bellingshausen Sea, Antarctica. *Cryosphere* 8, 2395–2407.

Geilfus, N.X., Galley, R.J., Crabeck, O., Papakyriakou, T., Landy, J., Tison, J.L., Rysgaard, S., 2015. Inorganic carbon dynamics of melt-pond-covered first-year sea ice in the Canadian Arctic. *Biogeosciences* 12, 2047–2061.

Gersonde, R., Zielinski, U., 2000. The reconstruction of late Quaternary Antarctic sea-ice distribution—the use of diatoms as a proxy for sea-ice. *Palaeogeogr. Palaeoclimatol. Palaeoecol.* 162, 263–286.

- Hall, B.L., Henderson, G.M., Baroni, C., Kellogg, T.B., 2010. Constant Holocene Southern-Ocean 14C reservoir ages and ice-shelf flow rates. *Earth Planet Sci. Lett.* 296, 115–123.
- Haslett, J., Parnell, A., 2008. A simple monotone process with application to radiocarbon-dated depth chronologies. *J. Roy. Stat. Soc.: Ser. C (Appl. Stat.)* 57, 399–418.
- Hawley, R.L., Waddington, E.D., Alley, R.B., Taylor, K.C., 2003. Annual layers in polar firn detected by borehole optical stratigraphy. *Geophys. Res. Lett.* 30.
- Hjort, C., Ingólfsson, Ó., Möller, P., Lirio, J.M., 1997. Holocene glacial history and sea-level changes on James Ross Island, Antarctic Peninsula. *J. Quat. Sci.: Publ. Q. Res. Assoc.* 12, 259–273.
- Lamping, N., Müller, J., Esper, O., Hillenbrand, C.-D., Smith, J.A., Kuhn, G., 2020. Highly branched isoprenoids reveal onset of deglaciation followed by dynamic sea-ice conditions in the western Amundsen Sea, Antarctica. *Quat. Sci. Rev.* 228, 106103.
- Lefebvre, W., Goosse, H., 2005. Influence of the Southern Annular Mode on the sea ice-ocean system: the role of the thermal and mechanical forcing. *Ocean Sci.* 1, 145–157.
- Lefebvre, W., Goosse, H., Timmermann, R., Fichefet, T., 2004. Influence of the Southern Annular Mode on the sea ice-ocean system. *J. Geophys. Res.: Oceans* 109.
- Lehmann, M.F., Bernasconi, S.M., McKenzie, J.A., Barbieri, A., Simona, M., Veronesi, M., 2004. Seasonal variation of the  $\delta C$  and  $\delta N$  of particulate and dissolved carbon and nitrogen in Lake Lugano: constraints on biogeochemical cycling in a eutrophic lake. *Limnol. Oceanogr.* 49, 415–429.
- Leventer, A., 1998. The fate of Antarctic "sea ice diatoms" and their use as paleoenvironmental indicators. *Antarctic sea ice. Biol. Process. Interact. Variability* 121–137.
- Leventer, A., Domack, E., Barkoukias, A., McAndrews, B., Murray, J., 2002. Laminations from the Palmer Deep: a diatom-based interpretation. *Paleoceanography* 17, PAL 3-1-PAL 3-15.
- Leventer, A., Domack, E., Pike, J., Stickley, C., Maddison, E., Brachfeld, S.A., Manley, P., McClennen, C., 2006. Marine Sediment Record from the East Antarctic Margin Reveals Dynamics of Ice Sheet Recession.
- Licht, K.J., Cunningham, W.L., Andrews, J.T., Domack, E.W., Jennings, A.E., 1998. Establishing chronologies from acid-insoluble organic 14C dates on Antarctic (Ross Sea) and arctic (north Atlantic) marine sediments. *Polar Res.* 17, 203–216.
- Maddison, E.J., Pike, J., Dunbar, R., 2012. Seasonally laminated diatom-rich sediments from Dumont d'Urville Trough, East Antarctic margin: late-Holocene neoglaciation sea-ice conditions. *Holocene* 22, 857–875.
- Maddison, E.J., Pike, J., Leventer, A., Domack, E.W., 2005. Deglacial seasonal and sub-seasonal diatom record from Palmer Deep, Antarctica. *J. Quat. Sci.: Publ. Q. Res. Assoc.* 20, 435–446.
- Maddison, E.J., Pike, J., Leventer, A., Dunbar, R., Brachfeld, S., Domack, E.W., Manley, P., McClennen, C., 2006. Post-glacial seasonal diatom record of the Mertz glacier polynya, East Antarctica. *Mar. Micropaleontol.* 60, 66–88.
- Massé, G., Belt, S.T., Crosta, X., Schmidt, S., Snape, I., Thomas, D.N., Rowland, S.J., 2011. Highly branched isoprenoids as proxies for variable sea ice conditions in the Southern Ocean. *Antarct. Sci.* 23, 487–498.
- McGregor, H.V., Evans, M.N., Goosse, H., Leduc, G., Martrat, B., Addison, J.A., Mortyn, P.G., Oppo, D.W., Seidenkrantz, M.-S., Sicre, M.-A., 2015. Robust global ocean cooling trend for the pre-industrial Common Era. *Nat. Geosci.* 8, 671–677.
- McKay, R., Colledge, N.R., Maas, S., Naish, T., Levy, R., Dunbar, G., Kuhn, G., 2016. Antarctic marine ice-sheet retreat in the Ross Sea during the early Holocene. *Geology* 44, 7–10.
- Meehl, G.A., Arblaster, J.M., Bitz, C.M., Chung, C.T., Teng, H., 2016. Antarctic sea-ice expansion between 2000 and 2014 driven by tropical Pacific decadal climate variability. *Nat. Geosci.* 9, 590.
- Meehl, G.A., Arblaster, J.M., Chung, C.T., Holland, M.M., DuVivier, A., Thompson, L., Yang, D., Bitz, C.M., 2019. Sustained ocean changes contributed to sudden Antarctic sea ice retreat in late 2016. *Nat. Commun.* 10, 14.
- Mezgec, K., Stenni, B., Crosta, X., Masson-Delmotte, V., Baroni, C., Braidà, M., Ciardini, V., Colizza, E., Melis, R., Salvatore, M.C., Severi, M., Scarchilli, C., Traversi, R., Udisti, R., Frezzotti, M., 2017. Holocene sea ice variability driven by wind and polynya efficiency in the Ross Sea. *Nat. Commun.* 8, 1334.
- Mortlock, R.A., Froelich, P.N., 1989. A Simple Method for the Rapid Determination of Biogenic Opal in Pelagic Marine Sediments, vol. 36, pp. 1415–1426. *Deep Sea Research Part A. Oceanographic Research Papers*.
- Narcisi, B., Petit, J.R., Delmonte, B., Scarchilli, C., Stenni, B., 2012. A 16,000-yr tephra framework for the Antarctic ice sheet: a contribution from the new Talos Dome core. *Quat. Sci. Rev.* 49, 52–63.
- Parkinson, C.L., 2019. A 40-yr record reveals gradual Antarctic sea ice increases followed by decreases at rates far exceeding the rates seen in the Arctic. *Proc. Natl. Acad. Sci. Unit. States Am.* 116, 14414–14423.
- Popp, B.N., Hanson, K.L., Dore, J.E., Bidigare, R.R., Laws, E.A., Wakeham, S.G., 1999. Controls on the carbon isotopic composition of phytoplankton. In: Abrantes, F., Mix, A.C. (Eds.), *Reconstructing Ocean History: A Window into the Future*. Springer US, Boston, MA, pp. 381–398.
- Popp, B.N., Laws, E.A., Bidigare, R.R., Dore, J.E., Hanson, K.L., Wakeham, S.G., 1998. Effect of phytoplankton cell geometry on carbon isotopic fractionation. *Geochim. Cosmochim. Acta* 62, 69–77.
- Reimer, P.J., Bard, E., Bayliss, A., Beck, J.W., Blackwell, P.G., Ramsey, C.B., Buck, C.E., Cheng, H., Edwards, R.L., Friedrich, M., 2013. IntCal13 and Marine13 radiocarbon age calibration curves 0–50,000 years cal BP. *Radiocarbon* 55, 1869–1887.
- Riaux-Gobin, C., Dieckmann, G.S., Poulin, M., Neveux, J., Labrune, C., Vétion, G., 2013. Environmental conditions, particle flux and sympagic microalgal succession in spring before the sea-ice break-up in Adélie Land, East Antarctica. *Polar Res.* 32, 19675.
- Riaux-Gobin, C., Poulin, M., Dieckmann, G., Labrune, C., Vétion, G., 2011. Spring phytoplankton onset after the ice break-up and sea-ice signature (Adélie Land, East Antarctica). *Polar Res.* 30, 5910.
- Salter, I., Kemp, A.E., Moore, C.M., Lampitt, R.S., Wolff, G.A., Holtvoeth, J., 2012. Diatom resting spore ecology drives enhanced carbon export from a naturally iron-fertilized bloom in the Southern Ocean. *Global Biogeochem. Cycles* 26.
- Schrader, H., Gersonde, R., 1978. Diatoms and silicoflagellates. In Zachariasse et al. *Microplaeontological counting methods and techniques—an exercise on an eight metres section of the lower Pliocene of Capo Rossello, Sicily*. Utrecht Micropal. Bull. 17, 129–176.
- Smik, L., Belt, S.T., Lieser, J.L., Armand, L.K., Leventer, A., 2016. Distributions of highly branched isoprenoid alkenes and other algal lipids in surface waters from East Antarctica: further insights for biomarker-based paleo sea-ice reconstruction. *Org. Geochem.* 95, 71–80.
- Smith, W., Anderson, R.F., Moore, J.K., Codispoti, L.A., Morrison, J.M., 2000. The US southern ocean joint global ocean flux study: an introduction to AESOPS. *Deep Sea Res. Part II Top. Stud. Oceanogr.* 47, 3073–3093.
- Stammerjohn, S.E., Martinson, D., Smith, R., Yuan, X., Rind, D., 2008. Trends in Antarctic annual sea ice retreat and advance and their relation to El Niño–southern oscillation and southern annular mode variability. *J. Geophys. Res.: Oceans* 113.
- Stenni, B., Curran, M.A.J., Abram, N.J., Orsi, A., Goursaud, S., Masson-Delmotte, V., Neukom, R., Goosse, H., Divine, D., van Ommen, T., Steig, E.J., Dixon, D.A., Thomas, E.R., Bertler, N.A.N., Isaksson, E., Ekaykin, A., Werner, M., Frezzotti, M., 2017. Antarctic climate variability on regional and continental scales over the last 2000 years. *Clim. Past* 13, 1609–1634.
- Stuiver, M., Polach, H.A., 1977. Discussion reporting of 14 C data. *Radiocarbon* 19, 355–363.
- Tanimura, Y., Fukuchi, M., Watanabe, K., Moriwaki, K., 1990. Diatoms in water column and sea-ice in Lützow-Holm Bay, Antarctica, and their preservation in the underlying sediments. *Bull. Natl. Sci. Mus. Ser. C* 16, 15–39.
- Tesi, T., Langone, L., Ravaoli, M., Giglio, F., Capotondi, L., 2012. Particulate export and lateral advection in the Antarctic polar front (southern Pacific ocean): one-year mooring deployment. *J. Mar. Syst.* 105, 70–81.
- Thomas, D.N., Kennedy, H., Kattner, G., Gerdes, D., Gough, C., Dieckmann, G.S., 2001. Biogeochemistry of platelet ice: its influence on particle flux under fast ice in the Weddell Sea, Antarctica. *Polar Biol.* 24, 486–496.
- Turner, J., Comiso, J.C., Marshall, G.J., Lachlan-Cope, T.A., Bracegirdle, T., Maksym, T., Meredith, M.P., Wang, Z., Orr, A., 2009. Non-annular atmospheric circulation change induced by stratospheric ozone depletion and its role in the recent increase of Antarctic sea ice extent. *Geophys. Res. Lett.* 36.
- Turner, J., Phillips, T., Marshall, G.J., Hosking, J.S., Pope, J.O., Bracegirdle, T.J., Deb, P., 2017. Unprecedented springtime retreat of Antarctic sea ice in 2016. *Geophys. Res. Lett.* 44, 6868–6875.
- Vorrath, M.E., Müller, J., Esper, O., Mollenhauer, G., Haas, C., Schefuß, E., Fahl, K., 2019. Highly branched isoprenoids for Southern Ocean sea ice reconstructions: a pilot study from the Western Antarctic Peninsula. *Biogeosciences* 16, 2961–2981.
- Wentworth, U., Chester, K., 1922. A scale of grade and class terms for clastic sediments. *J. Geol.* 30 (5), 377–392.